

2DPHOT: a multi-purpose environment for the two-dimensional analysis of wide-field images

F. La Barbera

INAF-Osservatorio Astronomico di Capodimonte, via Moiariello n.16, Napoli, Italy
 labarber@na.astro.it

R. R. de Carvalho

INAF-VSTCeN, via Moiariello n.16, Napoli, Italy¹
 reinaldo@das.inpe.br

J.L. Kohl-Moreira

Observatório Nacional, Rua General José Cristino 77, São Cristóvão, Rio de Janeiro 20921-400, Brazil

R.R. Gal

University of Hawaii, Institute for Astronomy, 2680 Woodlawn Dr., Honolulu, HI, 96822, United States

M. Soares-Santos

Instituto de Astronomia, Geofísica e Ciências Atmosféricas

M. Capaccioli

INAF-VSTCeN, via Moiariello n.16, Napoli, Italy

R. Santos

INPE/LAC, Av. dos Astronautas 1758, São José dos Campos, SP 12227-010, Brazil

N. Sant'Anna

INPE/LAC, Av. dos Astronautas 1758, São José dos Campos, SP 12227-010, Brazil

ABSTRACT

We describe 2DPHOT, a general purpose analysis environment for source detection and analysis in deep wide-field images. 2DPHOT is an automated tool to obtain both integrated and surface photometry of galaxies in an image, to perform reliable star-galaxy separation with accurate estimates of contamination at faint flux levels, and to estimate completeness of the image catalog. We describe the analysis strategy on which 2DPHOT is based, and provide a detailed description of the different algorithms implemented in the package. This new environment is intended as a dedicated tool to process the wealth of data from wide-field imaging surveys. To this end, the package is complemented by 2DGUI, an environment that allows multiple processing of data using a range of computing architectures.

Subject headings: Data Analysis and Techniques – Astronomical Techniques – Astrophysical Data – Galaxies

1. Introduction

In the past decade, wide-field surveys have provided the scientific community with a huge amount of spectroscopic and photometric data, allowing significant progress in our understanding of the Universe. Perhaps the most widely known example is the Sloan Digital Sky Survey (SDSS), whose sixth data release has now provided photometry in five bands for more than $2 \cdot 10^8$ astronomical objects, as well as spectra of about one million sources (see Adelman-McCarthy et al. 2007) over more than 8500 square degrees on the sky. One key to the success of the SDSS has been its capability to effectively store, process, and analyze, in a fully automated fashion, the vast amount of data gathered during survey operations. This goal was achieved by using dedicated and well-designed software pipelines, updated during survey operations with reprocessing for the delivery of new data releases. In the coming years, many general purpose astronomical surveys are slated to begin taking data. These wide-field imaging projects will gather deeper and deeper multi-waveband data over large sky areas, producing ever greater data flows. The scientific community must manage and analyze the huge wealth of information contained in these enormous datasets.

In this environment, we have undertaken the development of a new image analysis tool called 2DPHOT, designed to derive two-dimensional information by analyzing both the surface brightness distributions of individual astronomical sources and the spatial distribution of these sources in the image. The package includes several tasks, such as star/galaxy classification, measurement of both integrated and surface photometry of galaxies, PSF modeling, and estimation of catalog completeness and classification accuracy. The package is complemented by a graphical interface named 2DGUI. A schematic view of the 2DPHOT environment is shown in Fig. 1. Briefly, the environment is conceived as follows. To start processing, the input images are uploaded to a computer system (e.g. a local cluster or a grid computer) via the 2DGUI interface. 2DGUI also allows the user to configure the 2DPHOT input parameters. A scheduler is also included, allowing timed and

sequential execution of several 2DPHOT runs to be performed on the same computer. The actual image analysis is done by the 2DPHOT package, which is the core of the whole environment. During execution, several output tables and plots are produced, showing the different steps of the image analysis and providing a means of quality control. These data, which can also be directly downloaded from the user through the 2DGUI interface, are all uploaded into a database system (by the 2DLOAD application, see Fig. 1). This system produces a master catalog, by cross-matching 2DPHOT output results with information provided from other VO-compliant web services, and allows the user to perform data queries on this master catalog.

There are several survey projects for which the 2DPHOT environment has already been partly implemented or will be implemented. We have automatically processed the *g*- and *r*-band images from the Palomar Abell Cluster Survey (Gal et al. 2000), with the main goal of measuring structural parameters, i.e. the effective radius, the corresponding mean surface brightness, and the Sérsic index *n* of galaxies in clusters with different richnesses, in the redshift range of 0.05 to 0.2. The structural parameters have been used to estimate the environmental dependencies of internal color gradients in early-type galaxies (see La Barbera et al. 2005). Some examples of general purpose imaging surveys to be analyzed by 2DPHOT are those carried out with the VLT Survey Telescope (VST), a 2.6m diameter imaging telescope equipped with a large format (16k x16k pixels) CCD camera yielding a 1 square degree field of view. The VST, which will be located at the ESO Cerro Paranal Observatory (Chile), has been designed and constructed under a joint venture of ESO and the Capodimonte Astronomical Observatory (OAC). Several survey projects will be carried out with Capodimonte's VST guaranteed time².

One of the most interesting science cases for the development of 2DPHOT is the Kilo-Degree Survey with VST (KIDS, see Arnaboldi et al. 2007), a public survey project which will image 1500 square degrees of the southern sky in the *ugri* bands. As shown in a forthcoming paper (Soares-Santos et al. 2008), applying 2DPHOT to

¹On leave of absence INPE/DAS, Av. dos Astronautas 1758, São José dos Campos, SP 12227-010, Brazil.

²See <http://vstportal.oacn.inaf.it/>

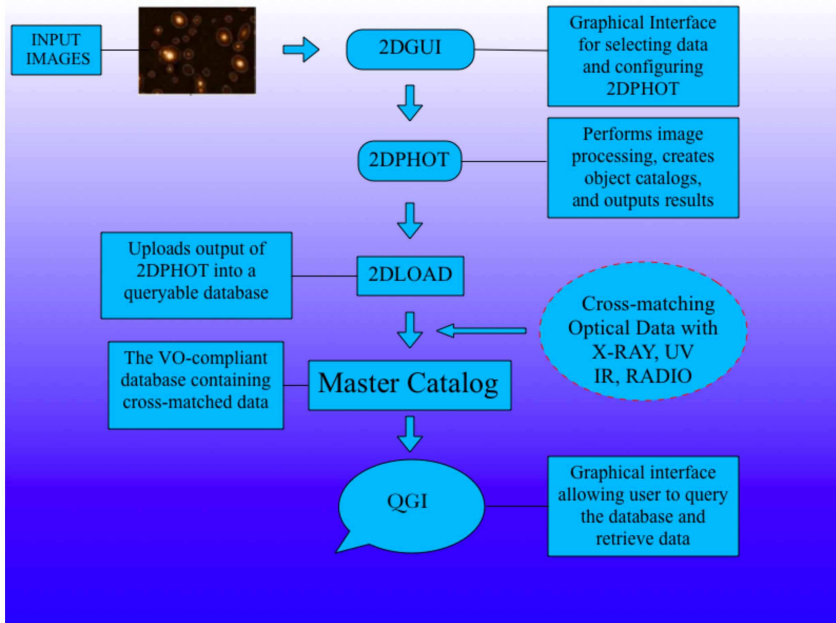


Fig. 1.— Schematic representation of the 2DPHOT environment.

a moderately deep survey such as VST-KIDS allows detection and measurement of massive galaxy clusters up to redshift $z \sim 1.2$ with high completeness. This cluster abundance measurement can be used to set strong constraints on the dark energy equation of state, which is one of the most crucial issues of modern observational and theoretical cosmology. Reliable star-galaxy separation, with accurate estimates of contamination at very faint flux levels, as well as an accurate cluster detection algorithm are among the 2DPHOT features of paramount importance for such a dark energy project.

This paper presents the 2DPHOT package³, describing the image analysis strategy on which it is based, as well as all the algorithms which are implemented for the different tasks the package performs. We also describe briefly the web-based graphical interface. This paper is intended as a reference work for all current and forthcoming scientific applications of 2DPHOT. The layout of the paper closely follows the order of ex-

ecution of the 2DPHOT tasks. In Sec. 2, we give general, short descriptions of these tasks, and how they are linked during image analysis. Section 3 describes the initial components of the first analysis step, i.e. how 2DPHOT produces the image catalog and identifies those objects which are classified as sure stars in the input image. The analysis of each source in the catalog is performed by extracting a stamp image from the input frame and constructing a corresponding mask file (Sec. 4). The package performs PSF modeling and derives rough structural parameters for all sources in the image as described in Secs. 5 and 6, respectively. Sec. 7 deals with the star/galaxy separation, while Sec. 8 describes the final fitting of galaxy stamps with seeing-convolved Sérsic models. The isophotal analysis of galaxy stamps is then described in Sec. 9, while the determination of the seeing-corrected galaxy aperture magnitudes is outlined in Sec. 10. Sections 11 and 12 describe how 2DPHOT estimates the completeness of the galaxy catalog and the uncertainty in the star/galaxy separation. Section 13 shows how 2DPHOT performs in estimating contamination and completeness at faint magnitudes. Finally, Sec. 14 presents the graphical interface (2DGUI).

³The source code of the package is available on request to the authors in its standard form, namely without the VO structure and 2DGUI interface, which will be made available in the near future.

A summary is given in Sec. 15. The input parameters and output quantities measured by 2DPHOT are provided in Appendices A and B, respectively.

2. The 2DPHOT package: tasks and analysis strategy

2DPHOT is designed to have a simple structure consisting of a shell script running a suite of C and Fortran77 programs developed using freely available software libraries. 2DPHOT works on both single-chip and wide-field (up to 16000x16000 pixels) images with a set of input parameters provided either at the invocation of the shell script through a command line syntax or a corresponding graphical interface (see Sec. 14). Thus, the package can be used either as a standalone application or via a dedicated web-based interface. The list of input parameters along with short descriptions is provided in Appendix A.

The main tasks of 2DPHOT are:

1. Producing a cleaned catalog of the image.
2. Performing reliable star/galaxy classification.
3. Estimating the completeness of the galaxy catalog and the contamination due to star/galaxy misclassification.
4. Constructing an accurate model of the Point Spread Function (PSF) of the input image, taking into account possible spatial variations of the PSF as well as deviations of stellar isophotes from circularity.
5. Deriving structural parameters of galaxies by fitting galaxy images with two-dimensional PSF-convolved Sérsic models.
6. Measuring galaxy isophotes by fitting them with Fourier-expanded ellipses, and derivation of one-dimensional surface brightness profiles of galaxies.
7. Measuring the growth curve of seeing corrected aperture magnitudes of galaxies.

All of these tasks are part of an image analysis flow and are strictly linked with each other such that the output from one task is used as input to the subsequent tasks. Figure 2 provides a graphical representation of this flow, where

the boxes represent different steps in the image analysis and the arrows follow the image processing timeline. The package starts by running S-Extractor (Bertin & Arnouts 1996) on the input image through an iterative procedure, allowing simultaneous measurement of the seeing FWHM and removal of spurious object detections. Stamp and mask images are then extracted for each object in the cleaned catalog, and are used to model the PSF across the field and to obtain a coarse estimate of the Sérsic parameters of the detected sources. Using both the S-Extractor stellarity index and the coarse effective radius estimates, 2DPHOT performs star/galaxy classification. The selected galaxies are then analyzed using a two-dimensional fitting procedure as well as a full isophotal analysis. Seeing corrected aperture magnitudes are also estimated. At this point, simulations are performed to estimate completeness and contamination of the final catalog.

The following sections describe all of the image analysis steps, following the diagram in Fig. 2. The output quantities measured by 2DPHOT are summarized in Appendix B.

3. The image catalog and the definition of ‘sure stars’

2DPHOT produces the source catalog from the input image using the S-Extractor package (Bertin & Arnouts 1996). Star/galaxy separation is performed on the basis of the S-Extractor stellarity index SI and the effective radius parameter r_e (see Sec. 7.1). In order to obtain a reliable estimate of the stellarity index, the seeing FWHM of the input image has to be provided to S-Extractor via the *SEEING_FWHM* input parameter (see the S-Extractor documentation⁴). To measure this, 2DPHOT produces a catalog from the input image via the following two-step procedure. S-Extractor is first run for the sole purpose of detecting sources in the input image and calculating their Kron magnitudes and FWHM and ELLIPTICITY parameters. By applying a 3σ clipping procedure to the FWHM and ELLIPTICITY distributions of all the bright ($S/N > 100$) unsaturated objects, 2DPHOT generates a preliminary list of candidate stars. The peak value f and the width σ of the FWHM distribution of

⁴http://terapix.iap.fr/rubrique.php?id_rubrique=91/index.html

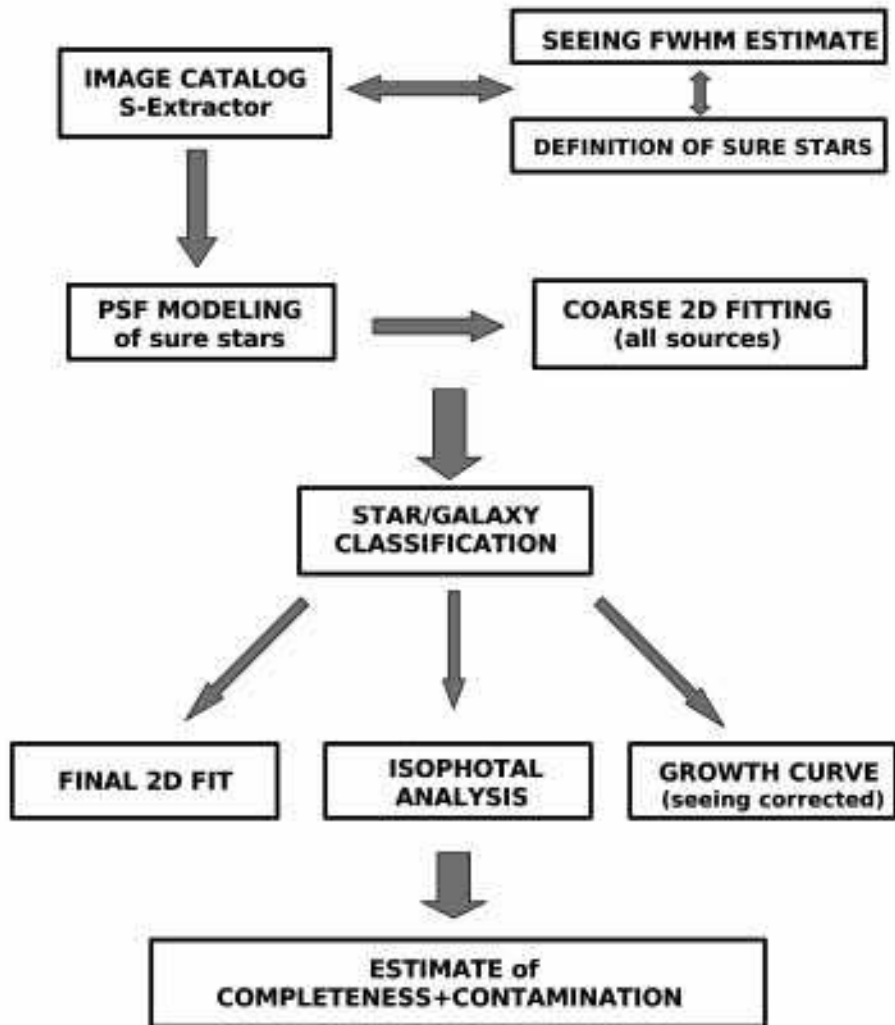


Fig. 2.— Image analysis flow of 2DPHOT.

these objects is derived using the bi-weight estimator (Beers et al. 1990). The values of f and σ define what we call the *sure star locus*, with the *sure stars* being the objects that lie within $\pm 2\sigma$ of f . Given the values of f and σ , S-Extractor is run a second time by setting the *SEEING_FWHM* parameter to the value of f . As an example of this procedure, Fig. 3 shows the FWHM versus S/N ratio diagram for all the detected sources in two CCD images of the galaxy cluster Abell 2495, which has been observed twice, under different seeing conditions, as part of the Palomar Abell Cluster Survey (Gal et al. 2000). Similar figures showing the sure star locus and the sure stars are automatically produced during each run of 2DPHOT.

After sure stars are defined, the catalog is cleaned of spurious detections by excluding all sources 3σ below the sure star locus. Objects whose distance from the image edges, in units of their FWHM value, is smaller than *REDGE*, where *REDGE* is one of the input 2DPHOT parameters (see Appendix A), are also excluded from the analysis since their photometry can be incomplete and/or corrupted.

4. Extraction of stamps and mask images

For each detected source, 2DPHOT extracts an image section (stamp) centered on the source. The area of the stamp is proportional to the *ISOAREA* output by S-Extractor such that a wide sky region around the central object is also included in the stamp. This allows a reliable estimate of the local background to be obtained from the two-dimensional fitting program (see Sec. 8). For each stamp, a mask image is also produced by flagging all the pixels that belong to all the other sources in the input image whose isophotal areas overlap the given stamp. The isophotal areas are defined through the *ISOAREA*, *ELLIPTICITY*, and position angle (*PA*) parameters from S-Extractor, by multiplying the *ISOAREA* value by an expansion factor *EXPND* (with a default value of 1.5), which is an input parameter of 2DPHOT. This expansion factor allows us to mask also the faintest diffuse external regions of each object. Sources whose isophotal areas overlap the central source by more than 50% are not masked out and are

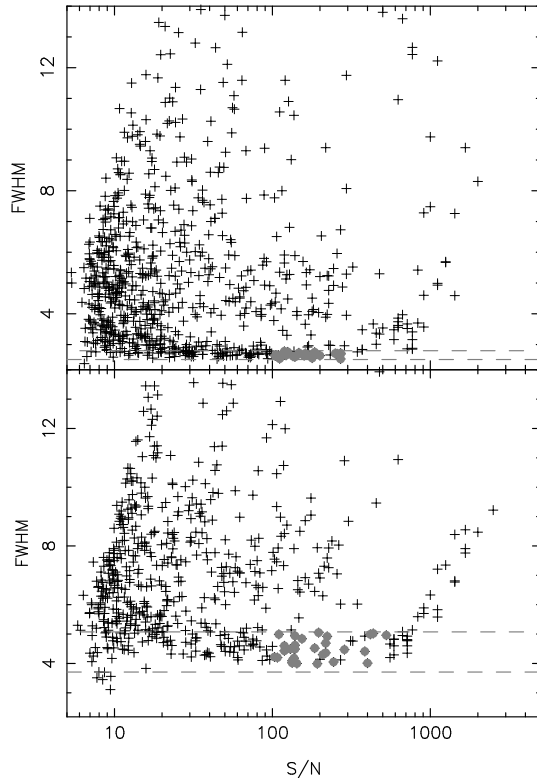


Fig. 3.— Locus of sure stars for two g -band images from the Palomar Abell Cluster Survey (see Gal et al. 2000). The images were obtained with a SITe 2048 \times 2048, AR-coated CCD, at the Palomar 1.5m telescope, and cover an area of 12.56' \times 12.56' around the cluster of galaxies Abell 2495 (at $z \sim 0.09$), with a pixel scale of 0.368 arcsec/pixel. Both panels plot the *FWHM* vs. S/N diagram for all the sources in the same field around the cluster center, with the lower panel for the image taken in worse seeing conditions ($FWHM \sim 1.7''$). The *FWHM* is given in pixel units. The S/N ratio is computed as the inverse of the uncertainty on the S-Extractor Kron magnitude (neglecting readout noise). The locus of sure stars is defined by the two horizontal dashed gray lines that mark the $\pm 2\sigma$ region around the peak value of the *FWHM* distribution of star candidates. Sure stars are defined as the bright ($S/N > 100$) non-saturated star candidates which lie inside the sure star locus, and are plotted as grey circles (see text).

analyzed simultaneously with the central object (see Secs. 6 and 8). For each stamp, the number of sources treated simultaneously is written into the *NOBJ* keyword of the corresponding mask file header. The local background value and its standard deviation are also estimated by applying biweight statistics to all the pixels which do not belong to the isophotal area of the central source and are not flagged in the mask file. These values are stored in the keywords *M_BK* and *S_BK* of the mask file header, respectively. Fig. 4 shows some examples of the stamp and mask images automatically produced by 2DPHOT.

5. PSF modeling

The Point Spread Function (PSF) is modeled by fitting the images of sure stars (Sec. 3) with a sum of two-dimensional Moffat functions. In order to account for PSF asymmetries, the isophotes of each Moffat function are described by ellipses, whose shape is modulated with a sin/cos angular expansion, similar to that adopted for describing deviations of the isophotal shape of early-type galaxies from pure ellipses (see e.g. Bender & Möllenhoff 1987). The number of fitted stars is given by the lesser of the number of available sure stars and the 2DPHOT input parameter *NSMAX*. The value of *NSMAX* is chosen as a compromise between the computation time for the fitting algorithm and the accuracy of the PSF model. Increasing *NSMAX* yields more accurate PSF models at the cost of larger computational times. Usually, values of *NSMAX* in the range of 3 to 5 give reliable results⁵. To account for possible spatial variations of the PSF across the chip, 2DPHOT provides two PSF modeling options. In the first case, a global PSF model is obtained by simultaneously fitting *NSMAX* stars randomly extracted from the entire list of sure stars. As a second option, 2DPHOT can construct a two-dimensional grid on the input image and derive a PSF model independently for each cell, by randomly selecting up to *NSMAX* stars among the available sure stars. PSF models are only derived for cells including at least two sure stars. The cell size has to be provided through the 2DPHOT

input parameter *NSIZE*. 2DPHOT associates to the PSF model of each cell the median values of the x and y coordinates of the corresponding fitted sure stars and the two-dimensional modeling of each galaxy (Sec. 8) is performed by using its closest PSF model. In order to avoid a discretely varying PSF across the chip, the user can also choose to adopt a locally interpolated PSF model. For each galaxy, 2DPHOT selects the PSF models of the cells around the galaxy itself, and performs a bi-linear interpolation of the selected models at the galaxy position. Since there is a strong correlation between the fitting parameters of each PSF model, 2DPHOT does not derive the local PSF model by interpolating each single fitting parameter. Instead, the interpolation is performed independently for each pixel of the PSF models, by interpolating the corresponding intensity values.

Prior to fitting the PSF, 2DPHOT applies a clipping procedure to remove stars that might be contaminated by nearby objects. For each star, all

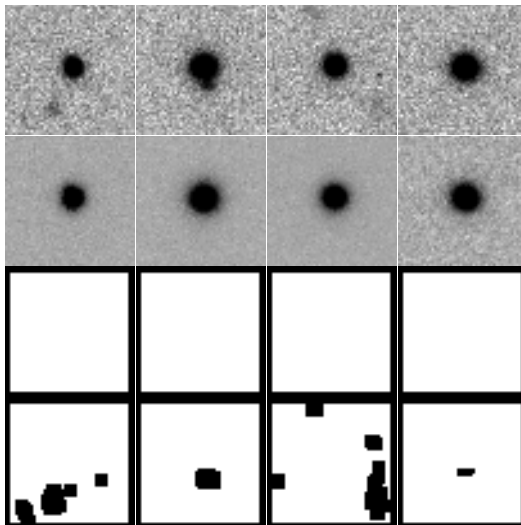


Fig. 5.— Examples of the clipping procedure applied to four stellar images. Each column corresponds to a different star. From top to bottom, the star stamps, the corresponding median images, the original mask images and the updated mask images are shown. The four stars have been selected because S-Extractor fails to detect the faint sources around them, and therefore the corresponding mask images are blank. The 2DPHOT clipping procedure detects the missed faint sources, and masks them in the updated mask images. The star stamps and median images use the same intensity scale.

⁵Processing several images, we found that increasing the value of *NSMAX* to more than 5 stars does not significantly change the output of 2DPHOT.

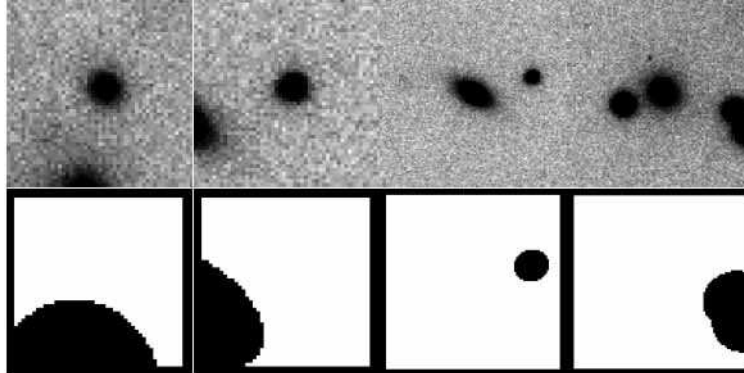


Fig. 4.— Examples of stamp and mask images produced by 2DPHOT. Stamps are shown in the upper panels, while lower panels plot the corresponding mask images. The pixels which are flagged in the mask files are plotted in black. Notice that pixels very close to the stamp edges are also flagged in each mask image. This is done to reduce computational overhead in the 2D fitting algorithm.

of the other sure stars are co-registered to the same center coordinates and median stacked. An rms image is constructed by estimating, at each position, the standard deviation of the stacked pixels. The mask images of the sure stars are then updated by flagging all the pixels which deviate by more than 5σ from the corresponding median images. If the fraction of flagged pixels is larger than 20% of the total mask image area, the sure star is considered to be strongly contaminated and it is excluded from the PSF fitting. This procedure allows faint sources which may not have been detected by S-Extractor to be masked, and to exclude objects which are misclassified or blended with nearby sources. Some examples of the clipping and mask update algorithms are shown in Fig. 5, while Fig. 6 plots an example of the PSF modeling results. The latter figure is automatically produced by 2DPHOT.

6. Coarse 2D fitting

2DPHOT produces an initial estimate of structural parameters for all objects in the input image using a discrete, coarse two-dimensional fitting algorithm (INI2DF). For each object, a set of PSF-convolved Sérsic models is constructed by varying the effective radius r_e , the total magnitude m_T , and the Sérsic index n . ‘Geometric’ parameters, such as the center coordinates, the axis ratio and the position angle of the models are estimated by fitting the object image with a single 2D Moffat

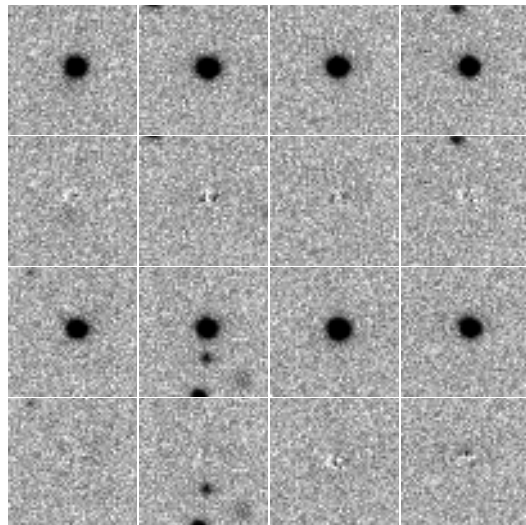


Fig. 6.— Examples of PSF modeling. Eight star images have been fitted simultaneously using a sum of three two-dimensional Moffat functions (see the text). For each star, two panels are shown, with the upper panel plotting the stamp image and the lower panel showing the fitting residuals.

function, and are kept fixed during the coarse fitting. The Moffat fit is performed by excluding the inner part of the object, which is strongly affected by seeing. The local background value is also not changed in the fit and is obtained from the keyword *M_BK* in the mask image header (see Sec. 4). INI2DF changes the effective radius of the Sérsic model using an adaptive grid of 10 values computed on the basis of both the pixel scale and the seeing FWHM of the image. Four different values are considered for the Sérsic index parameter, $n = \{1, 3, 5, 7\}$, while the total magnitude can take the values $m_T = m_K, m_K - 0.2, m_K - 0.4$, where m_K is the Kron magnitude of the source (S-Extractor *MAGAUTO*). We point out that the grids of r_e , m_T and n values have been empirically chosen by analyzing several images with a wide range of characteristics (e.g. optical and near-infrared data as well as ground-based and HST images). We found that further increasing the grid size does not change significantly the 2DPHOT results. With these sizes for the r_e , m_T and n grids, INI2DF produces a total of 120 discrete models, each of which is compared to the object image by computing the corresponding χ^2 value. The coarse structural parameters are given by the parameters of the model with lowest χ^2 .

In the case that, for a given stamp, several objects have to be treated simultaneously (see Sec. 4), the above procedure is modified as follows. A simultaneous fit is performed by using a single two-dimensional Moffat function for each object. Then, for each overlapping object, the others are subtracted using the fitted Moffat models. A corresponding updated mask image is also produced, by flagging all pixels for which the sum of the subtracted Moffat models exceeds the local background standard deviation (*S_BK* in the mask image header, see Sec. 4) by $> 50\%$. Coarse structural parameters are then obtained by fitting each object in the stamp as a single source, applying the same procedure outlined above. Some examples of this procedure are shown in Fig. 7. We see that there are some cases where the single Moffat models do not result in accurate subtraction of overlapping sources. Nevertheless, we found that the above approach allows reliable estimation of structural parameters, with the great advantage of significantly reduced computational times compared to an approach where overlapping

galaxy models are fitted simultaneously (see also Sec. 8).

7. Identification of stars in the 2DPHOT package

The classification of stars and galaxies is one of the most challenging issue in the analysis of astronomical images, and there is no method that works in all scenarios as the optimum classifier. In the current version, 2DPHOT adopts a simple method of star/galaxy (hereafter *S/G*) separation, which is based on both the S-Extractor and the coarse structural parameters estimated by the INI2DF procedure (Sec. 6). The parameters which are used for *S/G* classification have been chosen on the basis of Monte-Carlo simulations as detailed in Sec. 7.1, while the *S/G* classification algorithm is described in Sec. 7.2. In the future, we plan to implement more complex classification techniques (such as wavelet approaches), and provide a detailed comparison of their performance. Since there is no method that correctly classifies all sources in a given image, particularly at the faintest flux levels, it is crucial that every classification framework provide an estimate of contamination due to misclassified sources as a function of the S/N ratio. As described in Sec. 7.2, 2DPHOT accurately estimates such contamination using simulated stars and galaxies added to the input processed frame.

7.1. Reliable parameters to identify stellar sources

We adopt a two-step procedure to establish useful parameters for star/galaxy separation. First, we look for reliable classifiers of point-like sources, i.e. 2DPHOT output parameters whose values for stellar sources lie in a narrow region of parameter space over wide ranges of the S/N ratio, seeing, and sampling characteristics of the images. Then, we analyze the ability of such classifiers to separate stars and galaxies by examining the distribution of values they assume for both kinds of objects. To address the first point, we created simulated CCD images, each with a random spatial distribution of stars. The simulations were generated using the same pixel scale ($0.369''/pix$), image size (2048×2048 pixels), and the noise properties as the *r*-band images of the Palomar Abell Cluster

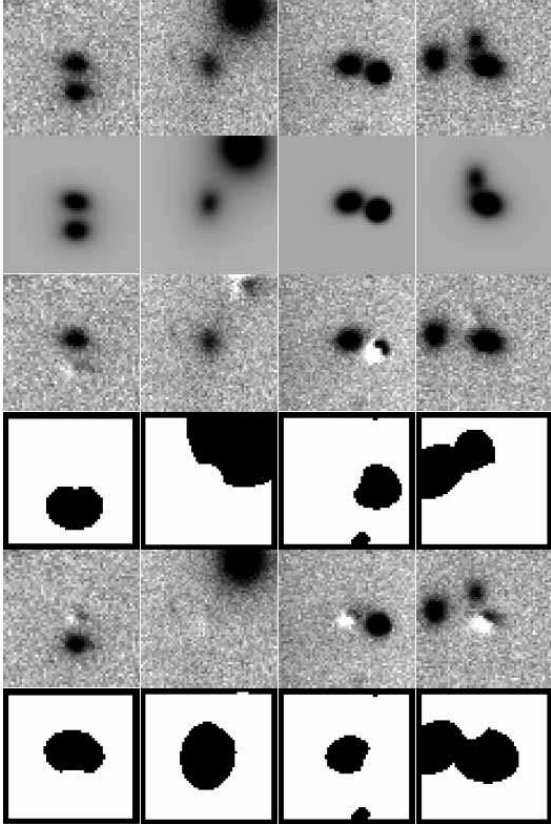


Fig. 7.— Coarse fitting of double objects. Panels in each column of the figure correspond to a different stamp image. From the top row down, the first and second rows show the stamp image and the corresponding Moffat model, obtained by simultaneously fitting two single Moffat functions. The third panel shows the subtraction of one Moffat function from the stamp. The corresponding updated mask image is shown in the fourth panel. The lowest two panels show the Moffat subtracted image and the corresponding updated mask image for the second object in the stamp.

Survey (hereafter PACS, see Gal et al. 2000). The PACS data have been extensively processed from the authors through the 2DPHOT package in order to investigate the effects of environment on internal color gradients of early-type galaxies (see La Barbera et al. 2005).

Stellar images were simulated using both the Gaussian profile and the Moffat law:

$$P(r) = \left[1 + \left(\frac{r}{r_c} \right)^2 \right]^{-\beta}, \quad (1)$$

where $P(r)$ is the surface brightness of the star as a function of the distance r to its center, β is the shape parameter of the profile, and r_c is the Moffat scale radius, which is related to the FWHM by $FWHM = 2r_c(2^{1/\beta} - 1)^{0.5}$. For the Moffat fits, we set $\beta = 3$, which is the mean value for stellar images in the PACS, and we varied the $FWHM$ from one star to another within each simulated image according to a normal deviate with central value $\langle FWHM \rangle$ and width σ_{FWHM} . Four simulated fields were created, labeled F1, F2, F3, and F4. The main simulation parameters are summarized in Table 1. For each field, we randomly created $N = 500$ stars, and we set the parameters $\langle FWHM \rangle$ and σ_{FWHM} as follows. For field F1, both the $\langle FWHM \rangle$ and σ_{FWHM} are set to the median values measured from the r -band PACS images. Fields F2 and F3 simulate observations with worse seeing conditions. F2 has the same $\langle FWHM \rangle$ as F1 while σ_{FWHM} is doubled, mimicking the case of large scatter in the seeing $FWHM$ across the image. Field F3 has the same σ_{FWHM} as field F1 but higher $\langle FWHM \rangle$, corresponding to either observations taken in worse mean seeing or data with better PSF sampling. Finally, for Field F4, we used the same $\langle FWHM \rangle$ and σ_{FWHM} values as F1, but stellar images were created with Gaussian profiles. We note that the above simulated images span all the possible cases that have been found when processing the PACS images, and because of their wide range of seeing parameters, they also reproduce the seeing properties of a variety of ground-based images.

Catalogs of the simulated stellar fields were generated as described in Sec. 3. For each field, all detected sources were fit with PSF convolved Sérsic models, following the procedure described

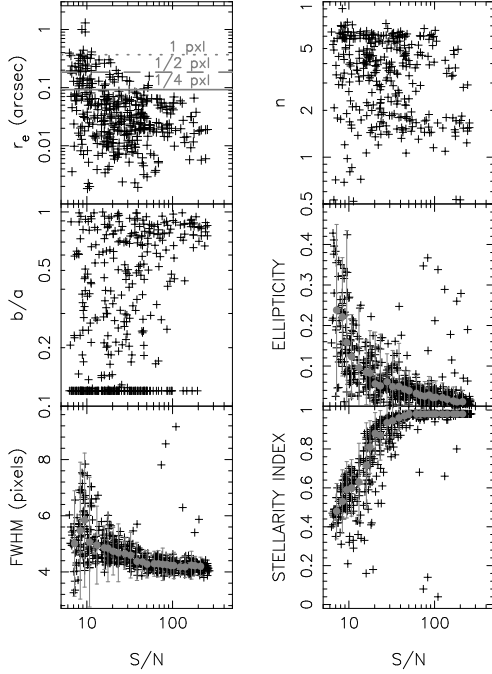


Fig. 8.— Measured parameters for sources in field F1 as a function of their S/N ratio. The quantities r_e , b/a , and n are the effective radius, axis ratio, and Sérsic index obtained from 2DPHOT through the two-dimensional fitting procedure (see Sec. 8). The other parameters (ELLIPTICITY, FWHM, and STELLARITY INDEX) are those measured by S-Extractor. As shown in the plot, the solid, dashed and short-dashed grey lines in the upper-left panel mark the values of r_e corresponding to different pixel fractions. Grey circles and corresponding error bars in the ELLIPTICITY, FWHM, and STELLARITY INDEX panels have been obtained by binning the data with respect to the S/N ratio, and correspond to the mean and 1σ interval in each bin.

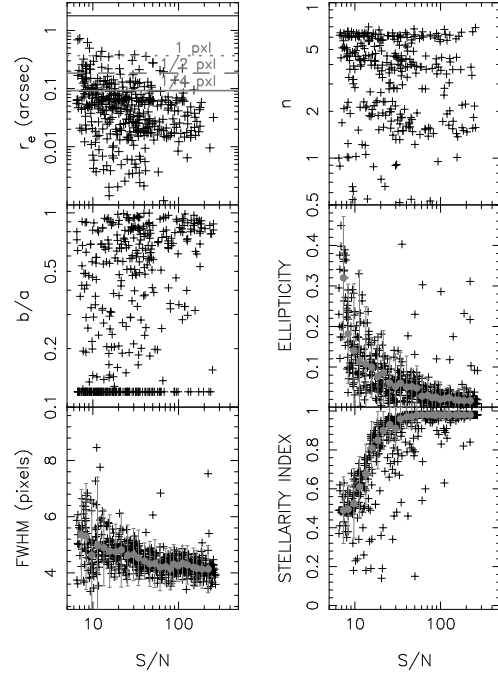


Fig. 9.— Same as Fig. 8 but for Field F2.

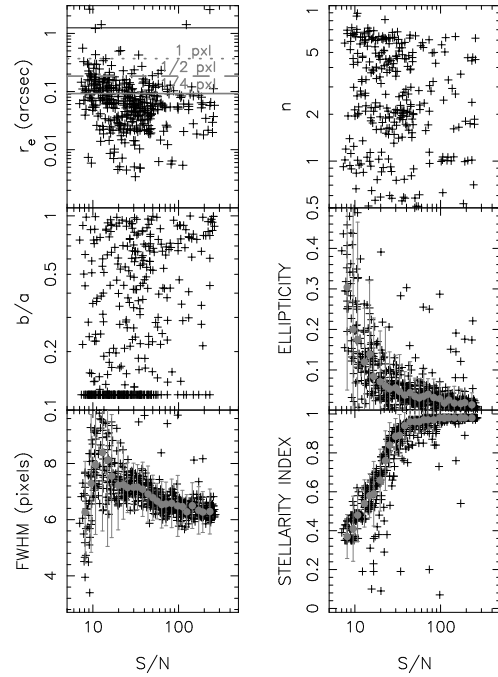


Fig. 10.— Same as Fig. 8 but for Field F3.

in Secs. 3–5 and running the final two-dimensional fitting program (see Sec. 8). Figs. 8, 9, 10 and 11 plot the Sérsic parameters, i.e. the effective radius r_e , the Sérsic index n , and the axis ratio b/a , as well as the the ELLIPTICITY, FWHM and stellarity index (hereafter SI) parameters from S-Extractor as a function of the S/N ratio of sources in fields F1, F2, F3, and F4, respectively. The S/N ratio was computed as the inverse of the uncertainty on the S-Extractor Kron magnitude. From Figs. 8, 9, 10 and 11, we draw the following conclusions:

- i) The Sérsic index and the b/a parameters are not reliable classifiers. The scatter in these quantities is large compared to the range of values they can assume.
- ii) The effective radius is a reliable classifier, in the sense that its values are always well limited to a given region of the corresponding parameter space. Whatever the seeing conditions are, the effective radius of stars is always smaller than ~ 1 pixel, and for $S/N > 30$, the values of r_e are always smaller than ~ 0.5 pixel.
- iii) As one would expect (Bertin & Arnouts 1996), the SI parameter of S-Extractor is a reliable classifier. Its values can range from 0 to 1, but for the simulated stars with $S/N > 20$, the values of SI are always larger than ~ 0.7 .
- iv) The FWHM and ELLIPTICITY parameters are good potential classifiers as well, although the values of FWHM are obviously strongly dependent on the seeing characteristics of the analyzed image. Generally, we find that using the FWHM and ELLIPTICITY parameters does not lead to any significant improvement in star/galaxy separation, and thus we elected not to use these parameters.

The reliability of the above star/galaxy separation scheme, based on the $SI-r_e$ diagram, will be further addressed in Section 13, where we will assess contamination and completeness as measured by 2DPHOT.

7.2. Final rules for identifying stellar sources

After INI2DF parameters have been derived for all the sources in a given field, 2PHOT performs S/G separation. Simulated images are constructed by adding a spatially random distribution of stars to the input image. The surface density of stars is chosen so that 50 stars are added to an input image area of 2000×2000 pixels, while the number of simulations is such that we have a total of 2000 artificial stars. Stars are created from the actual PSF model, with photon noise added based on the GAIN provided in the *default.sex* file of S-Extractor. The magnitude of each artificial star is extracted according to a uniform random S/N ratio distribution, with an upper cutoff of $S/N = 200$. For each simulation, a new catalog is generated and the SI parameter is computed for all of the artificial stars detected by S-Extractor. 2DPHOT defines star candidates on the basis of the distribution of these artificial stars in the SI versus magnitude diagram. First, artificial stars are ordered by ascending magnitude, and the 50 stars with magnitudes closest to that of each artificial star are selected. Then, for each artificial star, the 10% percentile of the distribution of SI values (SI_{10}) of the 50 selected artificial stars is computed. In order to minimize the number of galaxies that are misclassified at the faintest magnitudes of the catalog, a minimum cutoff of $SI_{10} = 0.7$ is imposed (see Sec. 12 for details). As a second option, that turns out to be more suitable in the case of deep images (see Sec. 13), 2DPHOT can define the star locus by applying the same procedure outlined above but replacing the 10% percentile of the SI distribution of simulated stars with the quantity $\theta - p\sigma$, where θ and σ are the location and width of the SI distribution, while p is a parameter input to 2DPHOT. With a suitable choice of p this second definition allows a narrower stellar locus to be defined in the SI versus magnitude diagram (see Sec. 12), and thus it can be more suitable at faint magnitudes where galaxies with small size are more likely to be misclassified as stars. Hereafter, unless stated explicitly, we will consider only the first definition of the star locus.

Since saturated stars have lower SI than bright unsaturated stars, at magnitudes brighter than those of artificial stars the value of SI_{10} is set

Table 1: Parameters of simulated stellar fields. Cols. 2, 3 and 4 give the $FWHM$, $\sigma_{FWHM}/FWHM$ and β parameters (see text). The gain, zero-point and read-out noise are in Cols. 5, 6 and 7, respectively. In the case of field 4, stellar images have Gaussian profiles.

$Field\#$	$FWHM$ (pxls)	$\frac{\sigma_{FWHM}}{FWHM}$ %	β	$gain$ e^-/ADU	$zpoint$	$rnoise$ e^-
1	4	3	3	1.62	30.75	6.3
2	4	3	3	1.62	30.75	6.3
3	6	6	3	1.62	30.75	6.3
4	4	3	Gaussian	1.62	30.75	6.3

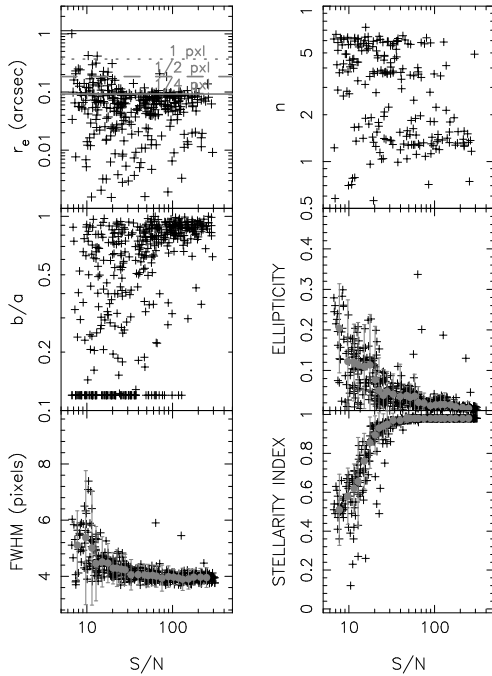


Fig. 11.— Same as Fig. 8 but for Field F4.

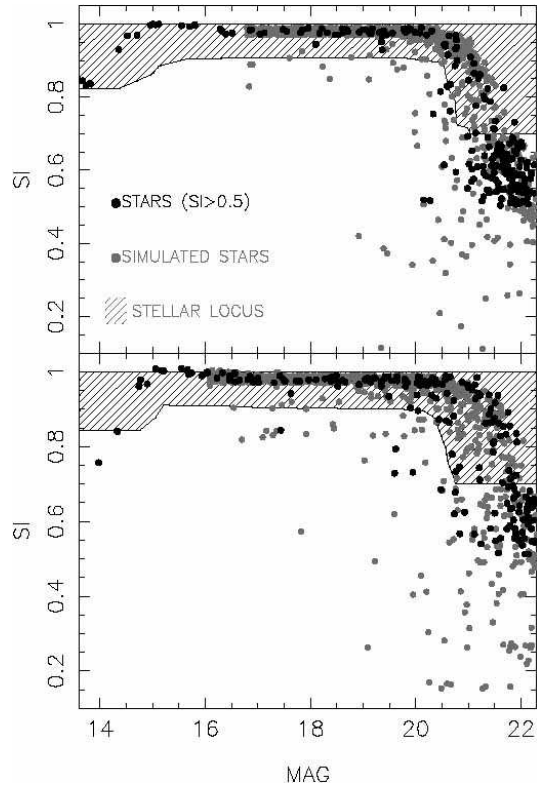


Fig. 12.— Definition of the stellar locus in the 2DPHOT package (see text). The plot shows the stellar index versus Kron magnitude diagram for two g -band images from PACS. Grey points are the simulated stars added to each field by 2DPHOT, while black circles show the objects with stellar index larger than 0.5. The hatched area marks the region used to select star candidates.

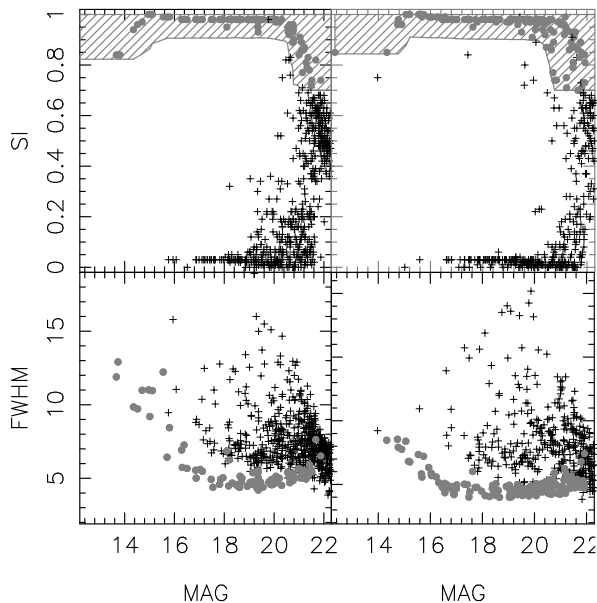


Fig. 13.— Selection of stars in 2DPHOT for two g -band images of the PACS. The upper panels show the stellar index versus Kron magnitude diagrams, with the hatched region showing the stellar locus (see text). Grey circles are the selected stars, while black crosses plot all the remaining sources. Lower panels show the corresponding FWHM versus Kron magnitude plots for the same PACS images.

to the minimum SI for observed sources with $SI > SI_{\min} = 0.5$. This procedure allows even saturated stars to be correctly classified by 2DPHOT. The value of SI_{\min} was chosen empirically based on several processed images where we found that saturated stars always have $SI > 0.5$, while the brightest galaxies all have lower SI . As shown in Fig. 12, star candidates are selected using the region between $SI = SI_{10}$ and $SI = 1$ in the SI versus magnitude diagram. Plots like those in Fig. 12 are automatically produced by each run of 2DPHOT. If required, the value of SI_{\min} can be changed by the user after inspection of the stellar locus plot. As final rules for S/G separation, we define an object as a candidate star if it belongs to the star candidate locus and its INI2DF effective radius is smaller than 1 pixel, with the latter criterion from the results of Monte-Carlo simulations discussed in Sec. 7.1. The locus of star candidates should include most of the point-like sources in the input image, with the percentage of misclassified objects increasing as the magnitude increases. The selection of stars through this procedure is shown in Fig. 13, where we consider two CCD images from the PACS. The plots in Fig. 13 are automatically produced by 2DPHOT. As one would expect, at faint magnitudes the star/galaxy classification becomes progressively more uncertain. The distribution of artificial stars with respect to the locus of star candidates provides a quantitative way to estimate the magnitude (and/or) the S/N limit above which the S/G classification is reliable (see Sec. 12).

8. Final 2D fitting

Objects identified as galaxies through the 2DPHOT S/G classification scheme are then fit with PSF convolved Sérsic models. This ‘final’ fitting differs from that of Sec. 6 since a full χ^2 minimization algorithm is adopted, without using any discrete (coarse) grid of reference convolved models (as for INI2DF), providing a precise estimate of structural parameters at the cost of longer computation times⁶. The χ^2 minimization is performed through the Levenberg-Marquardt algorithm, assigning zero weight to all the flagged pixels in the mask image. The 2D fitting routine

⁶The CPU time required for the final two-dimensional fitting is 4-5 times longer than for the coarse fit.

adopted in the 2DPHOT package is also described in La Barbera et al. (2002), where several tests of its accuracy have been performed. The initial conditions for the optimization routine are set to the output values of INI2DF, which are on average quite close to the best fitting final parameters. This largely reduces the well known issue of spurious convergence that can characterize strongly non-linear optimization problems. The case of overlapping objects is treated with an analogous approach to that described in Sec. 6 for the coarse fit. Instead of using the multiple single Moffat fits described in Sec. 6, 2DPHOT takes advantage of the INI2DF best fitting models to reduce the final fitting of overlapping objects to that of separate single sources. For each blended galaxy, the overlapping objects are subtracted using the INI2DF models and the mask image is correspondingly updated as described in Sec. 6. Although a suitable treatment of overlapping galaxies would require a simultaneous fit to be performed (see e.g. van Dokkum & Franx 1996), reducing the problem to that of fitting single sources greatly decreases computation times. Comparing both approaches, we verified that the 2DPHOT procedure does not produce any significant change in the final structural parameters of *multiple* objects. Some examples of two-dimensional fitting are shown in Fig. 14. The plots in this figure are automatically generated by 2DPHOT.

9. Isophotal analysis

To analyze the isophotal properties of galaxies, 2DPHOT performs an elliptical fit of galaxy isophotes and measures the deviations of such isophotes from purely elliptical shapes. Details on how the package performs these tasks are given in Sec. 9.1. The isophotal fit allows the radial surface brightness profile of galaxies and stars to be extracted. As described in Sec. 9.2, the package uses these brightness profiles to obtain a further estimate of the galaxy structural parameters, hence providing an independent estimate of these parameters than that obtained with the full two-dimensional fitting approach (Sec. 8). The isophotal analysis is also used to extract a growth curve for each galaxy’s aperture magnitude. The aperture magnitudes are computed and corrected for seeing effects as described in Sec. 10.

9.1. Isophotal fitting

For the measurement of galaxy isophotes, the package first defines the corresponding isophotal intensity values. For each stamp, a rough estimate of the object center coordinates are obtained as the intensity-weighted means of the x and y pixel coordinates. The mean values are computed in a section of 5x5 pixels around the intensity peak of the object. Using these center coordinates, a set of concentric circles is constructed, with radii equally spaced by 0.5 pixel. For each circle, the mean value of 90 intensity samples equally spaced in polar angle is computed via cubic interpolation of the stamp intensity values at the corresponding radial and polar coordinates. The mean intensity values provide an initial estimate of the object surface brightness profile, and are used to derive the isophotal contours of the object. This procedure allows us to construct isophotal contours whose equivalent radii are approximately equally spaced by 0.5 pixels. For a given isophotal intensity level, I , the isophote is defined by a set of x and y pairs on the stamp. These isophotal samples are defined as follows. For a given polar angle θ , different intensity values I_j are computed at several radii r_j from the galaxy center. The algorithm selects the smallest radius at which the intensity brackets the value of I (i.e. $I_j \leq I \leq I_{j+1}$ or $I_{j+1} \leq I \leq I_j$). The radius r corresponding to this intensity is then computed by linear interpolation of the r_j values with respect to I_j . The isophotal samples are directly computed from r and θ by varying θ such that the number of samples is proportional to the isophote length and by excluding those points flagged in the mask file. To exclude low signal-to-noise regions, the isophotal computation is stopped when the background-subtracted value of I falls below four times the background standard deviation within the stamp. As a default, to exclude galaxies whose isophotal contours are overly affected by seeing, 2DPHOT performs the isophotal analysis only for galaxies whose S-Extractor isophotal radius⁷ is larger than four times the seeing FWHM. Figure 15 plots some example of isophotal analysis for galaxies from one PACS r -band image. The panels shown in the plot are automatically produced by 2DPHOT.

⁷This is defined as $\sqrt{ISOAREA}/\pi$, where $ISOAREA$ is the $ISOAREA$ parameter of S-Extractor.

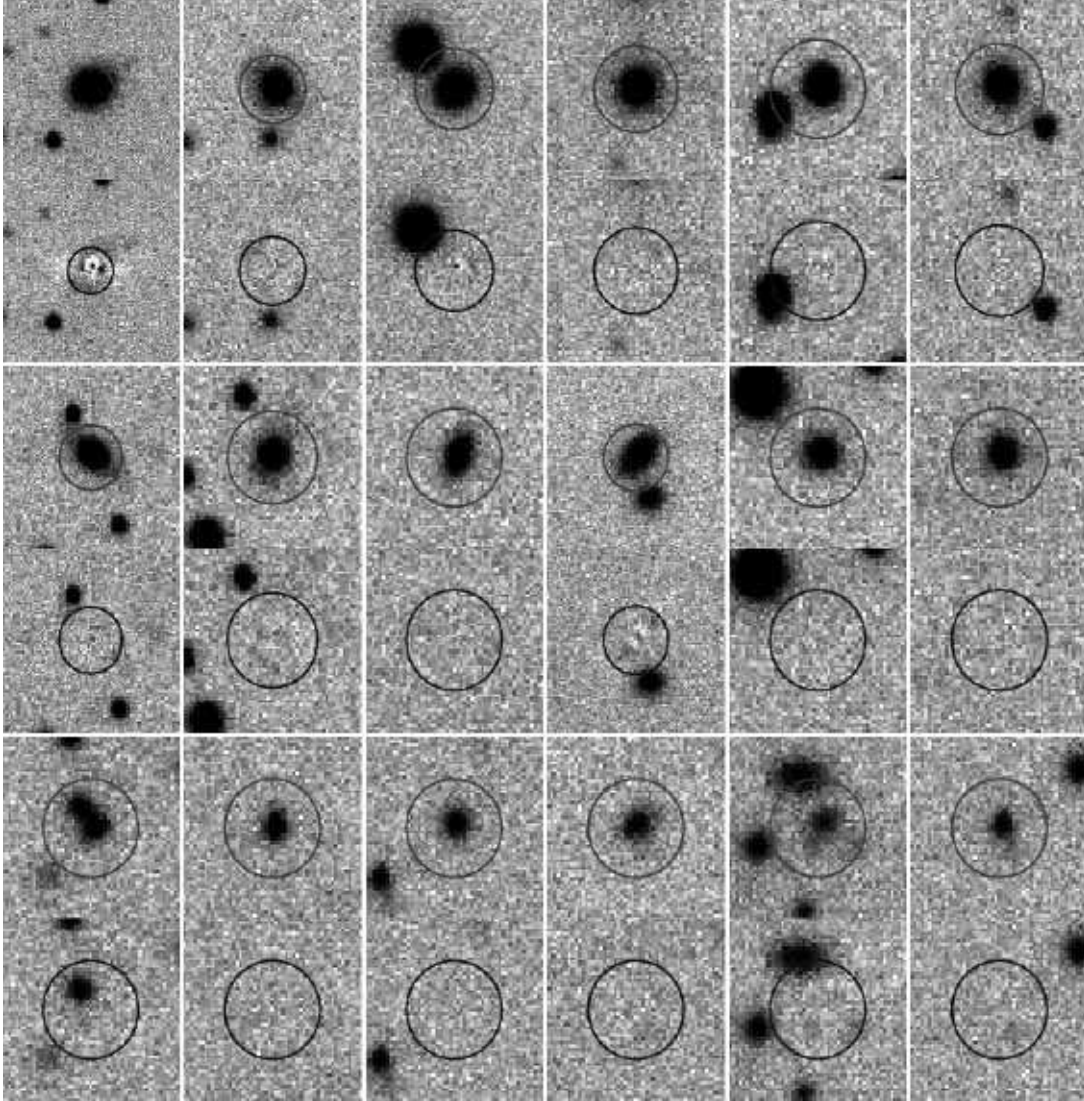


Fig. 14.— Two-dimensional fitting of galaxy stamps with seeing-convolved Sérsic models. Subpanels show the galaxy stamps and the corresponding residual images, obtained by subtracting the model fit from the galaxy stamp. For each galaxy stamp, the fitted galaxy is marked by a grey circle of radius $2''$, and the lower subpanel shows the residual image, where the same circle is plotted in black. From top to bottom and left to right, galaxies are shown in order of decreasing magnitude, from $r \sim 16.5$ for the upper-right panel to $r \sim 20$ for the lower-right panel. Images are drawn from the PACS image of the cluster Abell 574 at $z \sim 0.185$.

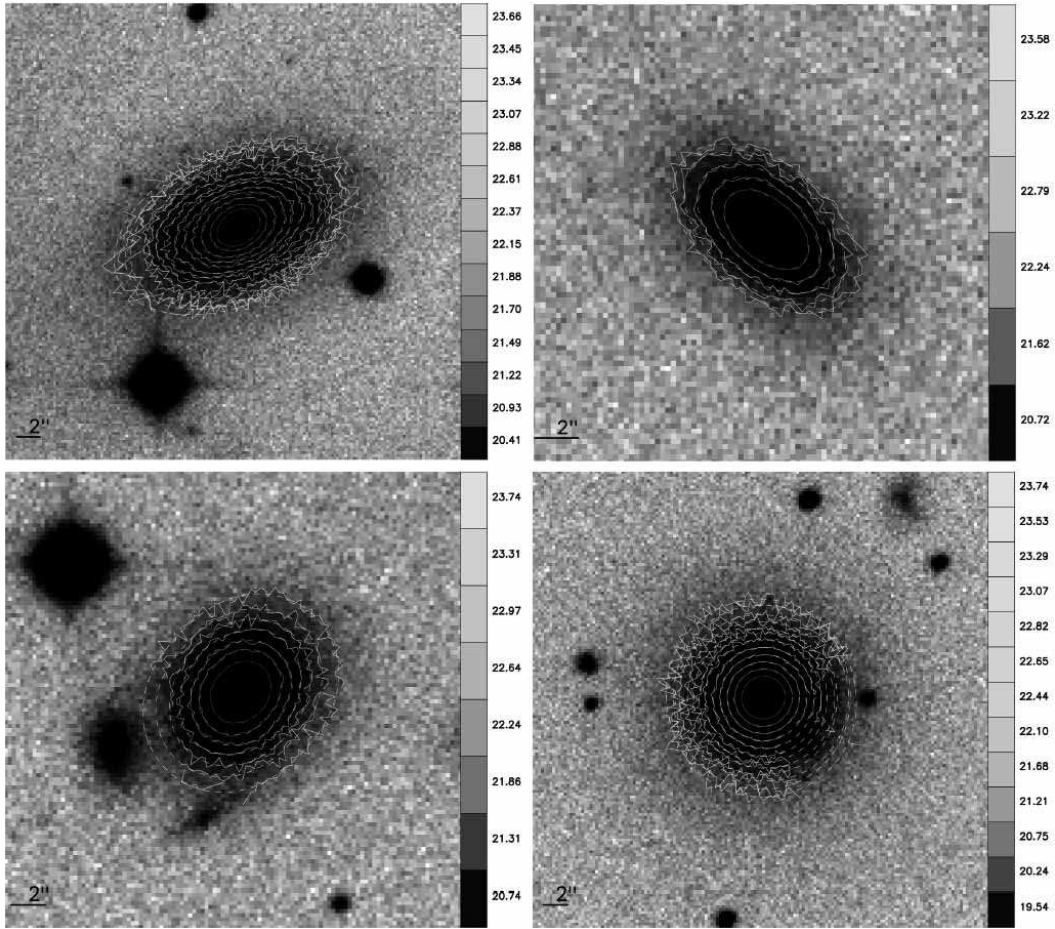


Fig. 15.— Fitting of galaxy isophotes with elliptical contours modulated by a series of sin/cos angular functions. The four panels plot different galaxy stamps, extracted from one PACS r -band image. Solid lines are the isophotal contours, derived as described in Sec. 9.1, while the fitted ellipses are plotted as dashed curves. The fits were performed by including only the a_4 term in the sin/cos expansion. Isophotes are plotted with different gray levels, with the grayscale proportional to the corresponding surface brightness value. The relations between gray intensity and surface brightness are shown on the grey scales at the right of each panel. Each surface brightness value on these gray scales corresponds to a different isophote. Surface brightness values are given in units of $mag/arcsec^2$, and become brighter as the isophotal color changes from white to black. The spatial scale is shown in the lower-left corner of each panel. The plots are produced automatically from the 2DPHOT package.

Galaxy isophotes are modeled as described in Bender & Möllenhoff (1987), by fitting each isophote with an elliptical contour modulated by the following sin/cos angular expansion:

$$\sum a_n \cdot \cos(n\theta) + b_n \cdot \sin(n\theta), \quad (2)$$

where θ is the polar angle, and the sum is done with respect to the index n . For $n \geq 3$, the coefficients a_n and b_n describe the deviations of the isophotes from the elliptical shape. In particular, the a_4 term is used to describe the boxy ($a_4 < 0$) and disky ($a_4 > 0$) isophotal shapes of early-type galaxies. Each ellipse is characterized by five fitting parameters, which are its center coordinates, equivalent radius, ellipticity, and position angle of the major axis. The sin/cos terms which have to be included in Eq. 2 are defined as input parameters of 2DPHOT. The isophotal parameters are derived by a χ^2 minimization procedure, through a Levenberg-Marquardt algorithm. Examples of isophotal fits are shown in Fig. 15, while Fig. 16 shows the radial profiles of isophotal parameters measured by the fitting procedure. All of these plots are automatically produced by 2DPHOT. Global values of a_n and b_n are computed as follows. Following Bender & Möllenhoff (1987) and Bender et al. (1989, hereafter B89), only the range of a_n and b_n profiles between a minimum radius R_{min} and a maximum radius R_{max} is selected. R_{min} is set to four times the seeing FWHM of the image, while R_{max} is set to twice the galaxy effective radius. The global a_n and b_n values are then defined as the average of their profiles within the selected radial range. Fig. 17 compares the a_4 values of B89 with those derived by running 2DPHOT on the r -band images of 42 galaxies from B89 with available photometry from the Sloan Digital Sky Survey Data Release 5 (SDSS DR5). Ten out of the 42 galaxies have been observed multiple times in the SDSS, and we used these repeated observations to check the reliability of the a_4 values. Looking at the figure, we see that there is good agreement between the two sets of measurements. Moreover, there is excellent agreement among repeated a_4 measurements. We note that 2DPHOT measures global a_n and b_n values somewhat differently than Bender et al. (1989), where either the peak values or the values of a_n and b_n at one effective radius were considered. Using the mean values has the advantage

of producing more robust estimates, reducing the effects of possible spurious peaks in the a_n and b_n profiles that can arise from noise fluctuations. Furthermore, as shown above, the two methods give, on average, fully consistent results.

9.2. Measuring surface brightness radial profiles

For all galaxies with final 2D fitting parameters, 2DPHOT extracts a one dimensional surface brightness profile. Four galaxy isophotes, corresponding to intensity values of 4, 6, 8, and 10 background standard deviations over the background level are computed, and are fitted by elliptical contours, as described in Sec. 9.1. The values of center coordinates, axis ratio, and position angle of the fitted ellipses are averaged, and are used to construct several concentric ellipses on the galaxy stamp, with their equivalent radii equally spaced by 0.5 pixel. The one dimensional surface brightness profile is then obtained as described in Sec. 9.1, by computing the mean intensity value in each ellipse as a function of the ellipse equivalent radius. The brightness profile is sky-subtracted by applying a similar procedure to that described in Jørgensen et al. (1995). The outermost part of the surface brightness profile intensities is fit with a power law, $\alpha \cdot r^{-\beta} + bg$, where the α and β parameters as well as the local background value, bg , are estimated by a χ^2 minimization procedure. The outermost part of the profile is defined as that radial range where the mean isophotal intensity minus an approximated median background falls below twice the background standard deviation. Some examples of surface brightness profiles for the same galaxies as in Fig. 15 are shown in Fig. 18. The profiles are used to obtain a further estimate of galaxy structural parameters independent of the 2D fitting approach. 2DPHOT follows the procedure described by Bendinelli et al. (1982, hereafter BPZ82). In this approach, one assumes the surface brightness distributions of both the galaxy and the PSF to have circular symmetry. With this assumption, it can be shown that the 2D seeing convolution is reduced to a one dimensional integral, with the integrand given by the product of the surface brightness radial profile of the galaxy model with that of the PSF surface brightness profile, modulated by a zero-order modified Bessel function (see

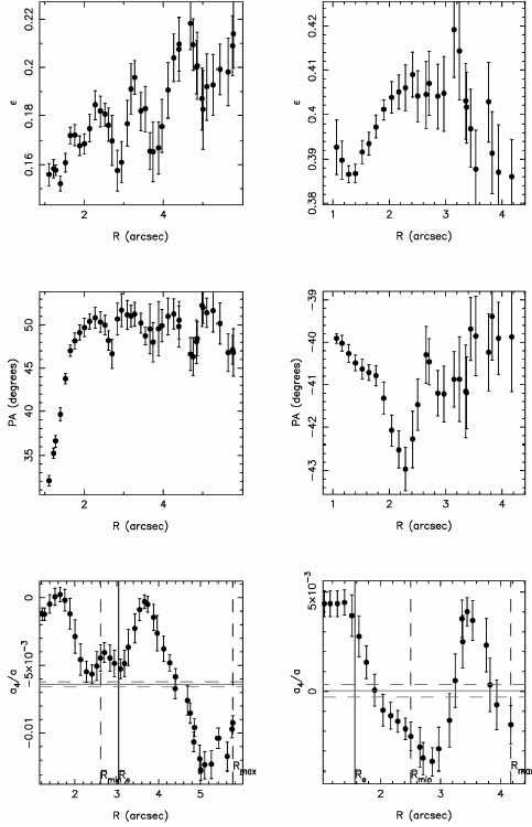


Fig. 16.— Radial profiles of isophotal parameters, as derived by the isophotal fitting algorithm (Sec. 9.1). From top to bottom, the panels show the profiles of ellipticity, position angle of the ellipse’s major axis, and a_4 coefficient as a function of the equivalent radius of the fitted isophotes. Left panels show the profiles of the galaxy in the lower-left panel of Fig. 15, while right panels correspond to the galaxy shown in the upper-right panel of Fig. 15. Error bars mark one sigma standard uncertainties. In the bottom panels, the minimum and maximum radii to define the global a_4 value are shown as vertical dashed lines. The effective radius of the galaxy is marked by a vertical solid line. The solid horizontal gray line denotes the mean value of a_4 in the selected radial range, while the dashed gray lines mark the corresponding 1σ interval.

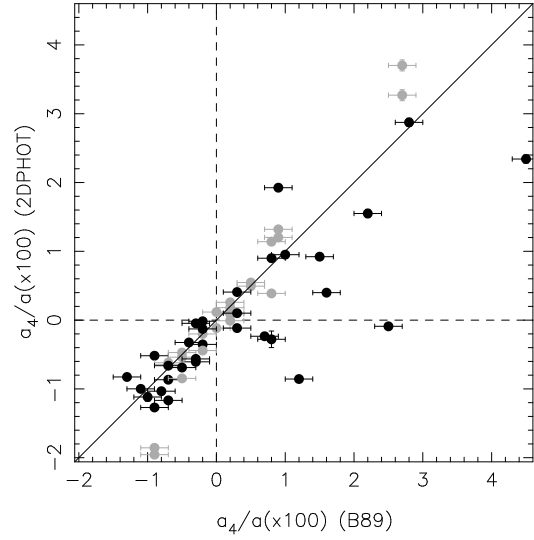


Fig. 17.— Comparison of a_4 values as estimated from Bender et al. (1989) (horizontal axis) and from the 2DPHOT package (vertical axis). The new a_4 values were obtained by running the 2DPHOT package on r-band images of the 42 galaxies of Bender et al. (1989) with available photometry from the SDSS DR5. The horizontal error bars mark the typical uncertainty on the a_4 values of Bender et al. (1989) (see their sec.2). The vertical bars denote one sigma standard uncertainties as estimated from 2DPHOT. Most of these error bars are smaller than the symbol size in the plot. From left to right, the following galaxies are plotted: NGC4261, NGC4365, NGC4387, NGC5322, NGC3605, NGC5127, NGC4478, NGC5532, NGC3894, NGC4551, NGC4406, NGC5576, NGC4649, NGC4374, NGC4472, NGC3842, NGC6411, NGC4636, NGC4489, NGC3608, NGC3640, NGC4486, NGC5638, NGC3379, NGC3193, NGC4494, NGC5490, NGC5831, NGC3613, NGC4382, NGC4168, NGC5845, NGC4125, NGC4473, NGC2693, NGC3377, NGC4621, NGC4550, NGC4564, NGC3610, NGC4660, NGC4251, NGC4570. In several cases, a galaxy has repeated SDSS observations. Such cases have been processed independently by 2DPHOT, and the corresponding values are plotted as gray symbols in the figure.

BPZ82 for details). Drawbacks and advantages of the one and two-dimensional methods have been discussed in many papers (see Kelson et al. 2000, La Barbera et al. 2002 and references therein). To summarize, the one dimensional approach allows one to significantly reduce the computation time of galaxy structural parameters. However, the uncertainties in the 1D parameters are larger, due to the circular symmetry approximation as well as to the interpolation of intensity values which is required to derive the galaxy and PSF one-dimensional profiles. On the other hand, the 2D approach is more time consuming, but allows more accurate estimates of structural parameters by taking advantage of all the information contained in the galaxy image. The one dimensional fitting procedure is included in the 2DPHOT package for completeness, particularly for cases where galaxy isophotes are strongly distorted and this distortion changes as a function of galaxy radius. In these situations the 2D approach can provide a poorly constrained fitting model, while useful parameters can still be obtained by the 1D approach. In order to apply the BPZ82 method, for each cell of the two-dimensional grid over which the two dimensional PSF modeling is done (see Sec. 5), a one dimensional PSF model is computed. To this end, the circular surface brightness profiles of all the sure stars in a given cell are derived (see Sec. 9.1) and averaged together after sky subtraction and flux scaling. The 1D combined profiles are fit with a sum of Moffat or Gaussian functions applying a procedure similar to that described in Sec. 5. The one dimensional structural parameters are then derived by the BPZ82 method, convolving one dimensional Sérsic models with the derived 1D PSF models. The best fitting 1D parameters, i.e. the central surface brightness, the effective radius and the Sérsic index are then derived using χ^2 minimization with the Levenberg-Marquardt algorithm. Examples of one dimensional fitting results are shown in Fig. 18 for the same galaxies as in Fig. 15.

10. Growth curves

The aperture magnitude growth curve of each galaxy is derived by direct integration of the corresponding one dimensional surface brightness profile. The integration is performed for each of the concentric ellipses used to extract the 1D profile.

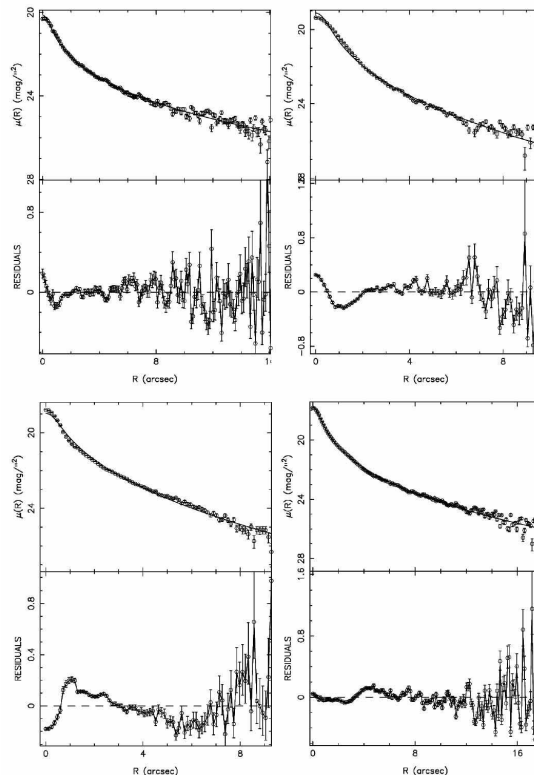


Fig. 18.— Surface brightness profiles of the same galaxies as in Fig. 9.1. In the upper plot of each panel, the surface brightnesses computed over different elliptical contours are plotted as a function of the ellipses’ equivalent radii. The surface brightness values have been sky subtracted as described in the text. The error bars denote 1σ uncertainties, computed by adding in quadrature the standard deviation of the intensity values in each ellipse with the uncertainty in the background estimate. The solid line is the best-fitting one dimensional Sérsic model. The lower plot of each panel shows the residuals, in units of $\text{mag}/\text{arcsec}^2$, obtained after subtracting the model from the data. The four panels correspond to the same galaxies as in Fig. 15.

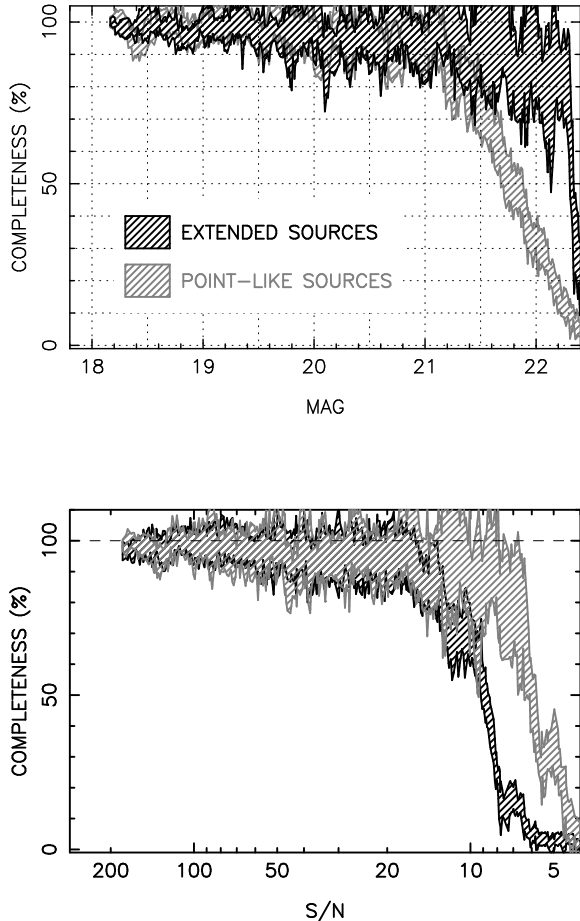


Fig. 19.— Completeness as a function of magnitude (upper panel) and S/N ratio (lower panel) for sources in the PACS image of the cluster Abell 1081 at $z \sim 0.16$. Hatched regions mark 1σ confidence intervals of the completeness. Stars and galaxies are plotted as grey and black regions, respectively, as shown in the upper panel. The dashed line in the lower plots marks the 100% completeness level.

As described in Sec. 9.2, all of the ellipses are defined by the average ellipticity and position angle of the galaxy. In order to correct the growth curve for seeing effects, the following procedure is adopted. The 2D seeing convolved Sérsic model obtained from the final 2D fitting analysis is used to extract a growth curve following the same procedure as for the galaxy image. The growth curve is also computed for the deconvolved Sérsic model, which is defined by the output parameters of the final 2D fit. The model is integrated over concentric ellipses using an adaptive 2D integration algorithm, and aperture magnitudes are extracted within the same apertures that define the galaxy growth curve. The difference between the growth curves of the seeing convolved and the seeing deconvolved models are used to correct the galaxy aperture magnitudes. We note that since the Sérsic model appears in the difference between the convolved and the deconvolved curves, the correction is expected to be largely independent of the choice of galaxy model, especially for the outermost parts of the galaxy where seeing corrections are small. The seeing corrected growth curve is used to estimate the half-light radius of the galaxy, and the corresponding mean surface brightness within that radius. We note that the seeing corrected growth curve and surface brightness profile allows the so-called eta function to be computed, which is defined by the ratio of the surface brightness value at a given radius to its mean value within the same radius (see Sandage & Perlmutter 1990). This function can be used to compute Petrosian metric radii and corresponding mean surface brightnesses. This feature will be implemented in the 2DPHOT package.

11. Completeness

In order to estimate the completeness of the galaxy catalog, we follow a procedure similar to that described in Sec. 7.2. 2DPHOT creates a set of simulated images by adding to the input image a random spatial distribution of artificial galaxies. The surface density of artificial galaxies in each simulated image and the total number of simulations are chosen using the same criteria outlined in Sec. 7.2. Artificial galaxies are created with seeing-convolved Sérsic models. The parameters of each model are chosen to match the distribution of galaxy structural parameters as a function of

galaxy magnitude obtained from the input image. The coordinates of each artificial galaxy are chosen randomly within the input image, while its total magnitude m_g is extracted from a uniform random distribution spanning the same range as the observed galaxies⁸. 2DPHOT randomly selects one of the fifty objects⁹ in the catalog with magnitudes closest to m_g and with corresponding S/N ratio larger than a cutoff value, S/N_{\min} . The INI2DF parameters of this object and the PSF model that correspond to the extracted center coordinates are then used to create the artificial galaxy. The S/N cutoff S/N_{\min} is introduced because at very low S/N ratios the catalog is highly incomplete, biasing the distribution of galaxy structural parameters toward objects with a higher detection probability, such as galaxies with smaller effective radii and/or higher central concentrations (i.e. higher Sérsic index). Since the distribution of galaxy parameters at magnitudes below the completeness limit is not known, we adopt the working assumption that this distribution is similar to that of galaxies which are ‘close’ to the completeness limit of the catalog. In other words S/N_{\min} is chosen as the lowest value of the S/N ratio for which the catalog is still nearly 100% complete. 2DPHOT adopts a default value of $S/N_{\min} = 25$. However, processing several images, we found that changing S/N_{\min} from 25 to 50 does not significantly change the completeness function.

For each simulated image, a catalog is generated using S-Extractor with the same settings as for the observed data. The galaxy completeness function is then derived by binning the artificial galaxies in magnitude and measuring the fraction of detected objects in each bin. The uncertainties on the completeness function are estimated by shifting magnitudes of artificial galaxies according to their corresponding uncertainties and re-computing the fraction of detected sources in each given bin. The same procedure is applied to the simulated stars created by 2DPHOT to define the locus of star candidates (Sec. 7.2). In this way,

⁸i.e. the same magnitude range as objects classified as extended sources by 2DPHOT

⁹This number is chosen to sample the full range of galaxy structural parameters at a given galaxy magnitude. For several kinds of images, we verified that varying this number from twenty to eighty does not affect significantly the completeness estimates.

the completeness functions of both extended and point-like sources are estimated. Fig. 19 shows the results of processing one r -band image from the PACS. The figure has been automatically produced by 2DPHOT. The completeness of the catalog is shown as a function of both magnitude and S/N ratio. For the latter, artificial data are binned by S/N ratio and the fraction of detected sources is measured in S/N bins. We see that both the galaxy and the star catalogs are almost 100% complete down to $S/N \sim 20$ ($r \sim 21^m$).

12. Contamination

Using simulated stars and galaxies described in Sec. 7.2 and Sec. 11, 2DPHOT estimates the fractions of galaxies and stars which are misclassified as a function of their magnitudes. We examine the distribution of the artificial galaxies and stars added to the input image in the SI versus magnitude diagram, using the definition of the star locus (Sec. 7.2) to perform S/G classification. This procedure is illustrated in Fig. 20, where the results obtained for one of the r -band PACS images are displayed. These figures are automatically produced by 2DPHOT. The upper panel shows the star locus as well as the distribution of both artificial stars and artificial galaxies in the SI - Mag diagram. We note that almost all of the artificial galaxies have $SI \leq 0.7$, which holds true for all images we processed with 2DPHOT. This implies that adopting a lower cutoff of $SI = 0.7$ for the definition of the star locus minimizes the fraction of misclassified galaxies at low S/N ratios, as noted in Sec. 7.2. The lower panel of Fig. 20 plots the fraction, ϕ_s , of misclassified stars, i.e. the fraction of artificial stars that lie outside the locus of star candidates, and the fraction, ϕ_g , of misclassified galaxies, i.e. the fraction of artificial galaxies that are classified as stars, as a function of their magnitude. We see that ϕ_g is always smaller than a few percent, while the fraction of misclassified stars increases rapidly at faint magnitudes ($MAG > 21$). For bright magnitudes, at $MAG < 20$, where one would expect that stars and galaxies are always properly identified, we find that the value of ϕ_s does not reach zero, but is typically $\sim 5\%$, varying from $\sim 3\%$ to $\sim 10\%$ between $MAG = 18$ and $MAG = 20$. In order to understand why there is such a small fraction of misclassified stars, we considered the PACS frame

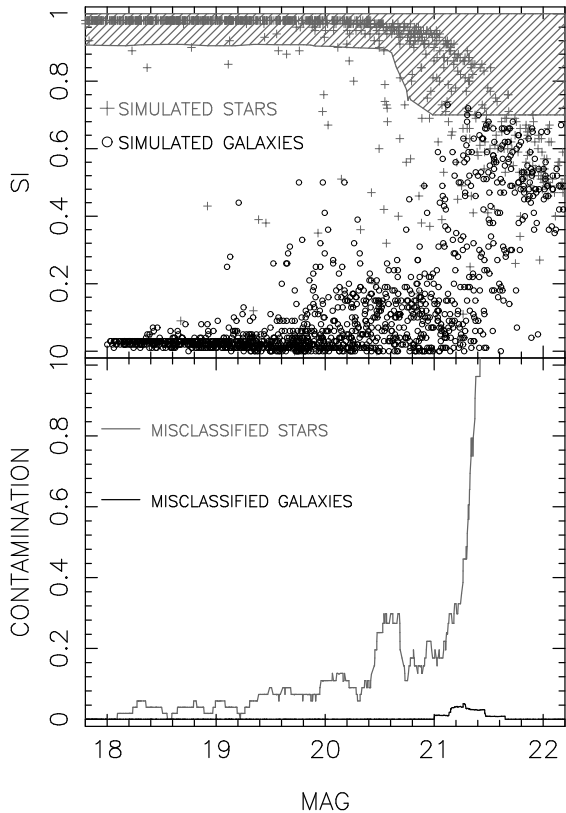


Fig. 20.— The upper panel plots the stellarity index from S-Extractor as a function of the Kron magnitude of simulated stars (grey crosses) and simulated galaxies (black circles), respectively. The hatched region corresponds to the stellar locus, which is defined as described in Sec. 7.2. The fractions of stars and galaxies that are erroneously classified on the basis of the stellar locus are plotted as grey and black curves, respectively. The plots have been obtained by processing the PACS image of the cluster Abell 1081, as for Fig. 19.

whose 2DPHOT contamination plots are shown in Fig. 20 and selected those misclassified stars for which $MAG \leq 20$, yielding 25 out of 726 total stars. Fig. 21 shows the regions where each of these 25 simulated stars are randomly added to the PACS image. The S-Extractor stellarity index and FLAG values are also reported in the plot. Looking at the figure, we can clearly see that the small misclassification fraction at the bright magnitudes is caused by blending. In fact, the figure shows that bright misclassified stars can be identified as follows: (i) they lie just on top of some other object in the field, (ii) strongly blended with bright galaxies, and (iii) embedded within the extended halo of a bright saturated star. We also find that for $\sim 70\%$ (18 out of 25) of the simulated stars the FLAG value estimated by S-Extractor is 3, corresponding to the case of blended sources (see Bertin & Arnouts 1996). We notice that the blending issue does in principle affect any star/galaxy separation algorithm, and can be more or less important depending on how crowded is the image being processed. On the other hand, adding simulated stars and galaxies to a given image as done by 2DPHOT (Sec. 7.2) one can estimate the star and galaxy contamination fractions by taking into account also misclassification due to blended sources.

13. Testing the star/galaxy separation at faint magnitudes

So far, we have tested the star/galaxy separation obtained with 2DPHOT using images from the Palomar Abell Cluster Survey. As shown in Sec. 12, with PACS data we achieve reliable star/galaxy separation down to $r \sim 21$. On the other hand, many scientific programs are expected to reach significantly deeper limits, where the small size of galaxies and blending issues can make the star/galaxy separation far more troublesome. In order to discuss how the star/galaxy separation in 2DPHOT performs at faint magnitudes, we use two deep i-band image pointings taken with the Large Format Camera (LFC) at the Palomar 200" telescope. Each LFC pointing covers a circular area of $24'$ in diameter, with a pixel scale of $0.182''/pixel$. Data for the same sky area were also taken with the Advanced Camera for Surveys (ACS) onboard of HST and consist of 15 pointings taken with the F814W filter. The ACS data were

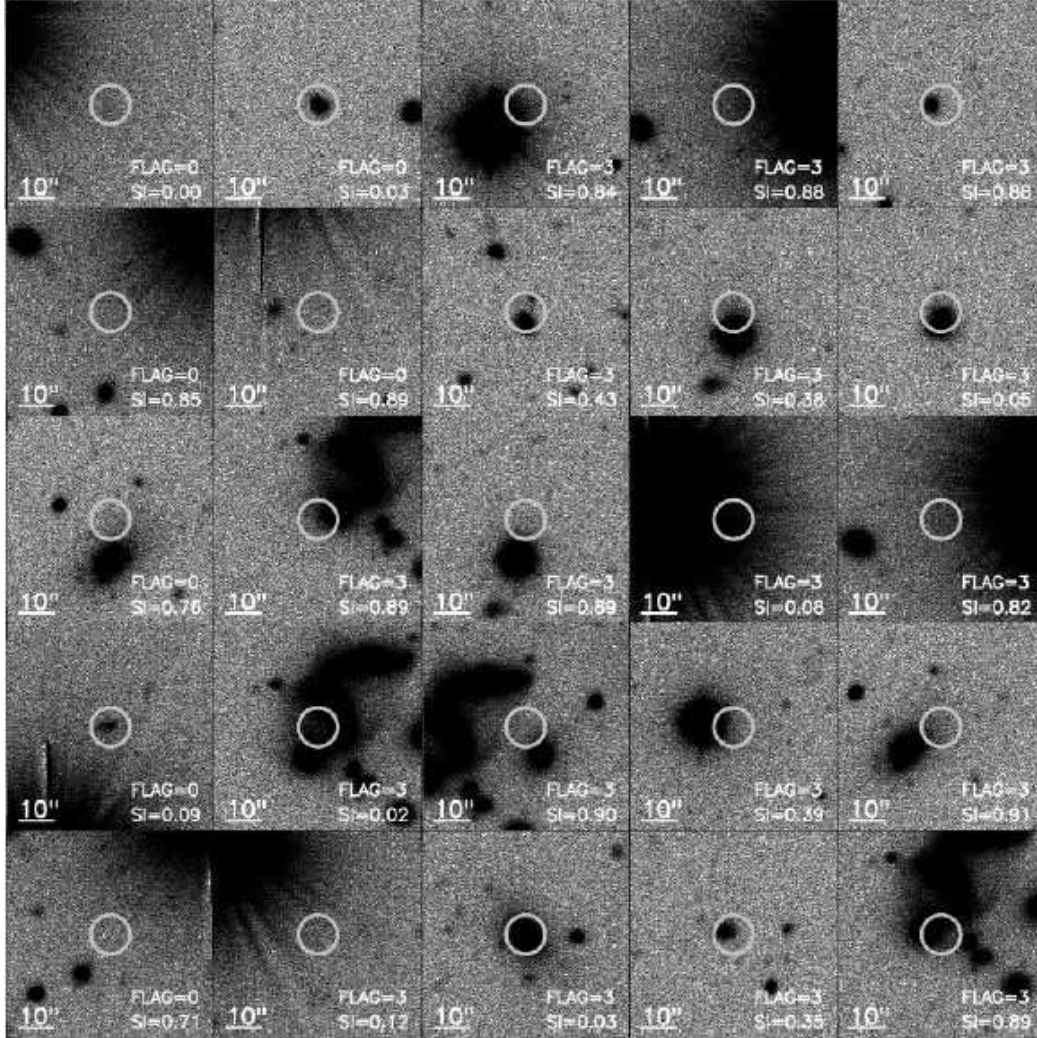


Fig. 21.— Regions of the same PACS image analyzed in Fig. 20 showing the position of bright simulated stars erroneously classified as galaxies by 2DPHOT (see the text). Each panel corresponds to a different simulated star. For clarity, we do not show the simulated star images added to the real one, but their positions on each panel are marked by a grey circle with a radius equal to three times the average FWHM value (1.8") of the PACS image. The stellarity index and the FLAG parameters estimated by S-Extractor are reported in the lower-right corner of each panel, while the spatial scale is shown in the lower-left.

drizzled to a pixel scale of $0.03''/\text{pixel}$, covering a total area of $\sim 13 \text{ arcmin}^2$. For more details on the data quality and main characteristics of the images, we refer the reader to Gal et al. (2005).

13.1. Comparing the HST and ground-based classification

We ran 2DPHOT on each of the ACS and LFC images and obtained the corresponding catalogs of stars and galaxies. All the ACS and LFC catalogs were matched, resulting in a final list of 3825 sources in common. In order to define the star locus, we adopted here the second option provided by 2DPHOT (see Sec. 7.2), where the locus is defined by setting the minimum value of the stellar index SI equal to $\theta - 2.5\sigma$, where θ and σ are the location and width values of the SI distribution of artificial stars. As shown in Fig. 22, where the star locus is plotted for one of the LFC and one of the ACS images, the above definition establishes a narrower stellar region reducing the number of small faint galaxies which can be potentially misclassified as galaxies.

As shown in Fig. 22, the HST data go about two magnitudes fainter than the LFC imaging. Moreover, HST allows a sharp separation of stars and galaxies down to $i_{AB} \sim 25$, while for LFC the two classes begin to overlap by $i_{AB} \sim 22$. Assuming that the HST data provide the 'true' classification, we can estimate the fraction of HST stars and galaxies which are not properly classified from LFC and compare these fractions with those estimated by 2DPHOT. Fig. 22 compares the 'true' misclassified fractions with those predicted by 2DPHOT, as computed by averaging those obtained for the two LFC fields. The figure shows that the 2DPHOT results are in good agreement with the 'true' contamination estimates. The fraction of misclassified galaxies is always very close to zero, reaching $\sim 10\%$ at $i_{AB} \sim 24$ for both the 'true' and 2DPHOT estimates. For stars, the fraction of both 'true' and 2DPHOT misclassified stars increases smoothly with magnitude, becoming larger than 50% at $i_{AB} \sim 24$. We notice that the 'true' fraction is slightly larger than that estimated by 2DPHOT in the magnitude range of $i_{AB} \sim 21$ to $i_{AB} \sim 23$. However, considering the uncertainty on the 'true' fraction of misclassified stars the above difference is only marginally significant. Hence, we conclude that also at the

fainter magnitudes sampled by the LFC photometry, 2DPHOT is able to provide reliable estimates of the contamination in the star and galaxy catalogs.

14. 2DGUI: An interface for 2DPHOT

The 2DPHOT package requires installation of supporting software packages¹⁰ and its performance varies depending on the compilers used. After installation, the user has to run the package by configuring both the input files for S-Extractor as well as some additional parameters specific to the package itself, which control the different steps of the image analysis (see Sec. 2). To simplify deployment and provide a uniform interface, we have developed a front-end called 2DGUI. To allow the timely execution of potentially time-consuming processing jobs and manage parallelization, we have also included a simple scheduler system.

The 2DGUI package consists of three basic components. First, we provide an interface where the user can execute several 2DPHOT runs (jobs) through a local 2DPHOT installation. Second, a small, local (i.e. server-independent) database provides user access to the output files of 2DPHOT. Finally, the simple scheduling system allows timely execution of several jobs to be performed without server overloading. All of these components were either developed or adapted from well-known, portable, royalty-free software. Since the database is included in the 2DGUI package, no additional software is required. Since the scheduler is based on the *cron* utility and on a bash- or csh-system shell, the server must use a Unix-like operating system.

The first step includes user identification and job creation through the form shown in panel 1 of Fig. 24. Currently, only data available on the server can be processed. After creating a job, the user must configure parameters for both S-Extractor and 2DPHOT, using the two forms shown in panels 2 and 3 of Fig. 24, respectively. Both forms show the command-line equivalent parameter names, their default values, and short comments. At this point, the job is created and scheduled, and information on the job execution is provided in the 2DGUI interface, as shown in

¹⁰such as S-Extractor and the *cfitsio* and *pgplot* libraries.

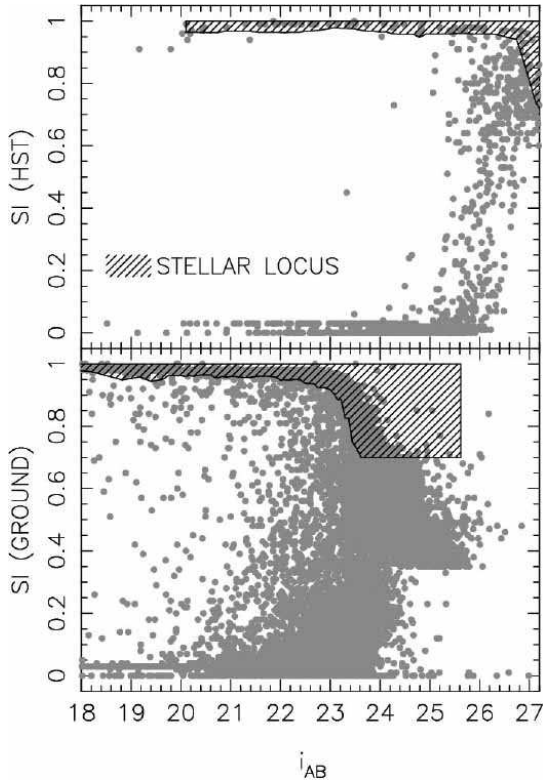


Fig. 22.— Definition of star locus obtained from 2DPHOT for one of the HST (upper panel) and one of the LFC (lower panel) images. Each panel plots the stellarity index versus the i_{AB} magnitude. Grey circles mark all the sources in a given image, with the corresponding stellar locus being represented by the hatched region.

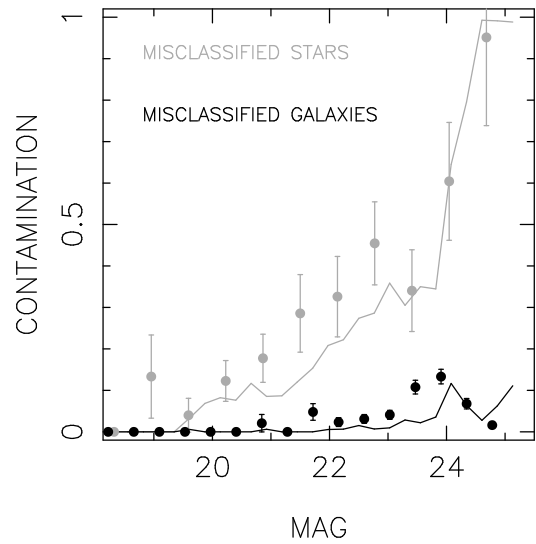


Fig. 23.— Comparison of the fractions of misclassified stars and galaxies provided by 2DPHOT with the 'true' values obtained by comparing the HST and LFC data (see text). The fractions of stars and galaxies are plotted in grey and black, respectively. The 'true' fractions are plotted as filled circles, with the error bars marking 1σ standard uncertainties, estimated by accounting for poissonian errors on counts in each magnitude bin. The fraction of misclassified sources provided by 2DPHOT are shown as continuous curves.

panel 4 of Fig. 24.

2DGUI then creates a user directory (if necessary), along with a subdirectory for each job defined by the user identification, the 2DPHOT and S-Extractor parameters, and the filename of the input image. Four files are stored in this directory: 1) the original FITS image uploaded by the user; 2) a shell script (*runme.sh*), that includes the command-line syntax¹¹ for running 2DPHOT; 3 and 4) The S-Extractor configuration and parameter files of S-Extractor, named *default.sex* and *default.param*.

During execution, the 2DPHOT main script dumps textual information on each step of the image analysis in a log file. 2DGUI reads this file and informs the user of the job processing status by automatically updating the form shown in panel 4 of Fig. 24. When processing is finished, all the files generated by 2DPHOT are listed in the 2DGUI interface, and the user can select and download 2DPHOT output results. The execution of several *runme.sh* files on a given server is done by a scheduling program which runs only a predefined maximum number of *runme.sh* scripts, in such a way as to avoid overloading the server.

Currently, 2DGUI is still under development and its components are actively being improved. The major planned improvements include the following features: 1) the ability for a given user to submit several jobs, using the same parameters to process several images simultaneously; 2) use of the local database to store users' preferred parameters; 3) offline processing alerts (e.g. sending an e-mail to the user when a task is completed); and 4) a remote dispatcher, that allows tasks to be executed remotely, e.g. on a local cluster or a grid computer.

15. Summary

We have presented 2DPHOT, a new computational tool for astronomical image processing, designed to analyze the output data of wide-field imaging surveys in a completely automated fashion. The package includes several tasks, such as star/galaxy classification, measurement of both integrated and surface photometry of galaxies, PSF modeling, estimation of catalog complete-

ness and classification accuracy. 2DPHOT incorporates a variety of quality control plots, which have historically been left to a separate step in image analysis, and is complemented by a graphical interface named 2DGUI. In addition, to accommodate the extensive output of 2DPHOT, both in terms of object catalogs and quality control figures, we are developing a database architecture which will comply with the standards proposed by the IVOA (International Virtual Observatory Alliance). All these components make 2DPHOT a powerful environment to analyze, handle, and store the output data coming from large area surveys. Some examples of surveys where we plan to apply this new analysis environment are those that will be carried out with the VLT-Survey Telescope (VST). We emphasize that 2DPHOT is conceived as a general purpose package, whose possible applications can span different research topics. In a forthcoming publication, we illustrate one such applications by describing a project to measure the abundance of clusters of galaxies at high redshifts (up to $z \sim 1.2$). Running 2DPHOT on simulated images of the VST KiloDegree Survey (KIDS, see Arnaboldi et al. 2007), we show that this cluster abundance can be measured with a high completeness level, allowing one to put strong constraints on the nature of dark energy in the Universe.

¹¹An example of this syntax is shown in panel 4 of Fig. 24.

2DGui

1 Job identification

Username	<input type="text"/>	
Password	<input type="password"/>	
FITS file	<input type="text"/> <input type="button" value="Browse..."/>	<input type="button" value="Next"/>

2DGui

2 SExtractor parameters

DETECT_MINAREA	<input type="text" value="10"/>	Minimum number of pixels above threshold
DETECT_THRESH	<input type="text" value="2"/>	<sigmas> or <threshold>, <ZP> in mag.arcsec-2
SATUR_LEVEL	<input type="text" value="32767"/>	level (in ADUs) at which arises saturation
MAG_ZEROPOINT	<input type="text" value="0"/>	magnitude zero-point
GAIN	<input type="text" value="2.5"/>	detector gain in e-/ADU
PIXEL_SCALE	<input type="text" value="0.396"/>	size of pixel in arcsec (0=use FITS WCS info).
READOUT	<input type="text" value="4"/>	readout noise.
		<input type="button" value="Next"/>

2DGui

3 2DPhot parameters

-i	<input type="text" value="10"/>	Minimum S/N ratio for surface photometry.
-p	<input type="text" value="OBJ_"/>	Prefix of galaxy names
-j	<input type="text" value="100"/>	Min S/N to select star candidates
-f	<input type="text" value="600"/>	Max S/N to select star candidates
-m	<input type="text" value="3"/>	Number of Moffat functions
-t	<input type="text" value="3"/>	Number of cos/sin terms
-b	<input type="text" value="0"/>	Cos terms to fit
-c	<input type="text" value="0"/>	Sin terms to fit
-d	<input type="text" value="-1000"/>	Min S/N ratio to fit cos/sin terms (default -1000=none)
-y	<input type="text" value="95"/>	XY size of PSF model
-e	<input type="text" value="2.5"/>	Minimum distance/FWHM ratio for objects to image edges
-r	<input type="text" value="10"/>	Minimum object separation for selecting stars
-s	<input type="text" value="15"/>	Maximum number of stars to perform PSF modeling
-a	<input type="text" value="0"/>	PSF fitting method (0=simultaneous, 1=single fitting, default 0)
-n	<input type="text" value="3000"/>	Cell size for local PSF modeling
-o	<input type="text" value="0"/>	if =1 only objects in the file list_obj are fitted
-v	<input type="text" value="99"/>	mag lim for Voronoi Tessellation (default 99=none)
-x	<input type="text" value="1.5"/>	Expanding factor of object stamps (default =1.5)
-z	<input type="text" value="401"/>	Maximum stamp size (default=401)
-j	<input type="text" value="1"/>	Number of Gaussian functions for 1D PSF fitting (default 1)
-g	<input type="text" value="0"/>	2D PSF functions (0=moffat, 1=gaussian) (default 0)
		<input type="button" value="Next"/>

2DGui

4 Your job is ready for execution.

Shell command: 2dphot -i 10 -p OBJ_ -j 100 -f 600 -m 3 -t 3 -b 0 -c 0 -d -1000 -y 95 -e 2.5 -r 10 -s 15 -a 0 -n 3000 -o 0 -v 99 -x 1.5 -z 401 -j 1 -g 0 f001458r60398.fits default.sex default.param

Your job is ready and was submitted to the scheduler.

Fig. 24.— Web forms used by the 2DGUI package. The upper form, panel 1, is used for the user login and image upload. The middle forms, panels 2 and 3, are used to set the S-Extractor and 2DPHOT parameters. The bottom form, panel 4, provides information to the user about the image processing.

A. Input parameters of 2DPHOT

Table 2 summarizes the main input parameters of 2DPHOT. These parameters can be either set as input options for the 2DPHOT main script or passed to the package by 2DGUI (see Secs. 2, 14). In the table, we also include a short description of each parameter, as well as a reference to the sections in this paper where the 2DPHOT task influenced by that parameter is described.

B. Output quantities measured by 2DPHOT

Table 3 summarizes the output quantities measured by 2DPHOT. A short description of all quantities is provided, together with a reference to sections where the corresponding 2DPHOT tasks are described. The quantities measured by running S-Extractor are not included for brevity.

Acknowledgements

We would like to thank Drs. Hugo Capelato, George Djorgovski and Scott Dodelson for careful reading of the paper and suggestions that helped improve the presentation. We also thank Drs. G. Busarello, C.P. Haines, P. Merluzzi, and M. Radovich for helpful comments and suggestions.

Table 2: Summary of 2DPHOT input parameters. Column 1: Options for the 2DPHOT main script. Column 2: Description of the parameter. Column 3: The name used to denote the parameter in the paper text. Column 4: Paper sections related to the parameter.

-l	Minimum S/N ratio required to perform 2D final fitting and surface photometry.		8, 9
-x	Stamp sizes are proportional to the S-Extractor ISOAREA parameter. This parameter provides the proportionality factor.	<i>EXPND</i>	4
-z	Maximum size of the stamp images. This parameter can be used to prevent overly large stamp frames.		4
-i	Minimum S/N ratio required to define sure stars.		3
-f	Maximum S/N ratio required to define sure stars.		3
-j	Number of Moffat/Gaussian functions for 1D PSF fitting.		9.2
-m	Number of Moffat/Gaussian functions for 2D PSF fitting.	<i>NSMAX</i>	5
-g	Functions used in the 2D PSF fitting (0=Moffat, 1=Gaussian).		5
-t	Number of cos/sin terms used for the expansion of star isophotes in the 2D PSF fitting.		5
-d	Minimum S/N ratio to perform 2D fitting with expansion of the galaxy model into a cos/sin series.		8
-b	Label providing the cos terms used for the expansion of the galaxy model in 2D final fitting (e.g. -b 34 makes 2DPHOT calculate the a_3 and a_4 coefficients)		8, 9.1
-c	Label providing the sin terms used for the expansion of the galaxy model in 2D final fitting.		8, 9.1
-e	Minimum distance of an object to the image edges, in units of its FWHM. Objects that are closer to the edge this distance are not analyzed.	<i>REDGE</i>	3
-s	Maximum number of sure stars used in a cell to perform PSF modeling.	<i>NSIZE</i>	5, 9.2
-a	Flag that determines the 2D PSF fitting method. When equal to zero, this option forces all sure stars in a given cell to be fitted simultaneously. When equal to one, a single fit to each sure star is performed.		5
-n	Size (in pixels) of the grid cells where PSF modeling is performed.		5
-o	The user can choose to process only some objects in the image by providing a list of x and y coordinates on the image. This feature is enabled with -o 1.		3

Table 3: Summary of 2DPHOT output quantities. Column 1: Quantity description. Column 2: Related sections in the text.

S-Extractor quantities.	3, 4
Stellar locus quantities: stellar index vs. S/N ratio for S/G separation, mean and standard deviation values of the sure star locus.	3, 4, 7
PSF fitting parameters: central intensity, width, axis ratio, position angle, shape parameter (in the case of PSF fitting with Moffat functions), and cos/sin terms of each PSF fitting function; central coordinates and local background value of each sure star stamp; reduced χ^2 of PSF fitting. These quantities are obtained for both the 2D and 1D fitting methods.	5, 9.2
Coarse Sérsic parameters: center coordinates, central surface brightness, effective radius, axis ratio, position angle of the major axis, Sérsic index, total magnitude.	6
Final 2D fitting parameters: center coordinates, central surface brightness, effective radius, axis ratio, position angle of the major axis, Sérsic index, total magnitude, local stamp background value, reduced χ^2 .	8
Isophotal parameters. For each isophote, the following quantities are computed: center coordinates, equivalent radius, position angle of the major axis, coefficients of the sin/cos expansion.	9
1D Sérsic fitting parameters: central surface brightness, effective radius, Sérsic index, total magnitude, reduced χ^2 .	9.2
Seeing corrected parameters: aperture magnitudes and surface brightness values corresponding to elliptical and circular contours, half-light radius and the corresponding mean surface brightness is also computed, petrosian function.	10
Completeness function: percentage of recovered simulated stars and galaxies as a function of the S/N ratio and magnitude.	11
Contamination estimates: percentages of misclassified stars and galaxies as a function of the S/N ratio and magnitude.	12

REFERENCES

- Adelman-McCarthy J. K. et al., 2007, submitted to The Astrophysical Journal Supplement Series
- Arnaboldi, M. et al., Messenger No. 127, March 2007, pp.28-32
- Bender, R., & Möllenhoff, C. 1987, A&A 177, 71
- Bender, R. et al. 1989, A&A 217, 35
- Bendinelli, O., Parmeggiani, G., & Zavatti, F. 1982 Ap&SS, 83, 239
- Bertin, E., & Arnouts, S. 1996, A&A 117, 393
- Gal, R.R., de Carvalho, R.R., Brunner, R., Odewahn, S.C., & Djorgovski, S.G. 2000, AJ 120, 540
- Gal, R.R., Lubin, L.M., & Squires, G.K. 2005, AJ, 129, 1827
- Jørgensen, I., Franx, M., & Kjaergaard, P. 1995, MNRAS 273, 1097
- Kelson, D., Illingworth, G.D., van Dokkum, P.G., & Franx, M. 2000, ApJ 531, 184
- La Barbera, F., Busarello, G., Merluzzi, P., Maszarotti, M., & Capaccioli, M., 2002, ApJ 571, 790
- La Barbera, F., de Carvalho, R.R., Gal, R.R., Busarello, G., Merluzzi, P., Capaccioli, M., & Djorgovski, S.G. 2005, ApJ, 626, 19
- Lopes, P.A.A., et al. 2004, AJ 128, 1017
- Sandage, A. & Perlmutter, J.M. 1990, ApJ 350, 481
- Shewchuk, J. 1996, in Applied Computational Geometry, ed. M.C. Lin & D.N. Manocha (Berlin: Springer), 203
- Soares-Santos, M., de Carvalho, R.R., La Barbera, F., Lopes, P., Kohl-Moreira, J.K., Gal, R.R., Capaccioli, M. 2007, ApJ *to be submitted*
- van Dokkum, P. G., & Franx, M. 1996, MNRAS 281, 985